Feedbacks between the formation of secondary minerals and the infiltration of fluids into the regolith of granitic rocks in different climatic zones (Chilean Coastal Cordillera)

Ferdinand J. Hampl[1], Ferry Schiperski[1], Christopher Schwerdhelm[2], Nicole Stroncik[3], Casey Bryce[4], Friedhelm von Blanckenburg[3,5], Thomas Neumann[1]

[1]Department of Applied Geochemistry, Technische Universität Berlin, Ernst-Reuter-Platz 1, 10587 Berlin, Germany
[2]Geomicrobiology Group, Eberhard-Karls-University Tübingen, Schnarrenbergstrasse 94-96, 72076 Tübingen, Germany
[3]Earth Surface Geochemistry, GFZ German Research Centre for Geosciences, Telegrafenberg, 14473 Potsdam, Germany
[4]School of Earth Sciences, University of Bristol, Wills Memorial Building, Queens Road, Bristol BS8 1RJ, United Kingdom
[5]Institute of Geological Sciences, Freie Universität Berlin, Malteserstrasse 74-100, 12249 Berlin, Germany

Correspondence to: Ferdinand J. Hampl (ferdinand.j.hampl@tu-berlin.de)

Abstract. Subsurface fluid pathways and the climate-dependent infiltration of fluids into the subsurface jointly control the intensity and depth of mineral weathering reactions. The products of these weathering reactions (secondary minerals), such as Fe(III) oxyhydroxides and clay minerals, in turn exert a control on the subsurface fluid flow and hence on the development of weathering profiles.

We explored the dependence of mineral transformations on climate during the weathering of granitic rocks in two 6 m deep weathering profiles in Mediterranean and humid climate zones along the Chilean Coastal Cordillera. We used geochemical and mineralogical methods such as (micro-) X-ray fluorescence, oxalate/dithionite extractions, X-ray diffraction and electron microprobe mapping to elucidate the transformations involved during weathering. In the profile of the Mediterranean climate zone, we found a low weathering intensity affecting the profile down to 6 m depth. In the profile of the humid climate zone, we found a high weathering intensity. Based on our results, we propose mechanisms that can intensify the progression of weathering to depth. The most important is weathering-induced fracturing (WIF) by Fe(II) oxidation in biotite and precipitation of Fe(III) oxyhydroxides, and by swelling of interstratified smectitic clay minerals that promotes the formation of fluid pathways. We also propose mechanisms that mitigate the development of a deep weathering zone, like the precipitation of secondary minerals (e.g., clay minerals) and amorphous phases that can impede the subsurface fluid flow. We conclude that the depth and intensity of primary mineral weathering in the profile of the Mediterranean climate zone is significantly controlled by WIF. It generates a surface-subsurface connectivity that allows fluid infiltration to great depth and hence promotes a deep weathering zone. Moreover, the water supply to the subsurface is limited in the Mediterranean climate and thus most of the weathering profile is generally characterized by a low weathering intensity. The depth and intensity of weathering processes in the profile of the humid climate zone, on the other hand, are controlled by an intense formation of

34 secondary minerals in the upper section of the weathering profile. This intense formation arises from pronounced dissolution

35 of primary minerals due to the high water infiltration (high precipitation rate) into the subsurface. The secondary minerals, in

36 turn, impede the infiltration of fluids to great depth and thus mitigate the intensity of primary mineral weathering at depth.

37 These two settings illustrate that the depth and intensity of primary mineral weathering in the upper regolith are controlled by

38 positive and negative feedbacks between the formation of secondary minerals and the infiltration of fluids.

39

40 **Keywords:** Coastal Cordillera, feedback, weathering-induced fracturing, secondary minerals, Critical Zone, fluid flow

41 1 Introduction

42 The formation of weathered material (regolith) from unweathered rock (bedrock) is a key process for shaping Earth´s surface.

43 It is of major importance for making mineral-bound nutrients accessible to the biosphere of the Critical Zone (e.g., Dawson et

44 al., 2020) and to supply rocks and minerals to the sediment cycle. In this process the in-situ disaggregation and chemical

45 depletion of weathered rock (saprock) to saprolite plays an essential role. This transformation is a result of fracturing and

46 mineral dissolution (e.g., Navarre-Sitchler et al., 2015). Both are associated with chemical, physical (e.g., Goodfellow et al.,

47 2016), and biological weathering processes (e.g., Drever, 1994; Lawrence et al., 2014; Napieralski et al., 2019). These

48 processes are linked to climate-related parameters such as precipitation rate, fluid flow (water and gases), and biological

49 activity. Apart from that, the weathering processes and hence the saprolite formation also depend on primary fractures (e.g.,

50 Molnar et al., 2007; Hynek et al., 2017; Kim et al., 2017; Holbrook et al., 2019; Hayes et al., 2020; Krone et al., 2021; Hampl

51 et al. 2022a), discontinuity density and tortuosity (Israeli et al., 2021), thermoelastic relaxation (e.g., Nadan and Engelder,

52 2009) as well as the topographic surface profile (e.g., Rempe and Dietrich, 2014; St. Clair et al., 2015). However, one of the

53 most fundamental parameters for the regolith formation is the mineral content of the bedrock. The weathering of some of these

54 primary minerals and the consequent formation of secondary minerals can lead to an amplification of the depth and intensity

55 (i.e., the parameter describing the elemental loss and relative amount of secondary minerals) of primary mineral weathering

56 (e.g., Fletcher et al., 2006; Lebedeva et al., 2007; Buss et al., 2008; Behrens et al., 2015; Hampl et al. 2022a). Such mechanisms

57 comprise (1) a forcing process like the formation of secondary minerals that is triggering (2) a responsive process such as more

58 intense infiltration of fluids to depth. The latter process reinforces the initial forcing process of secondary mineral formation.

59 Such a mechanism is therefore called positive feedback between (1) and (2). The formation of secondary minerals can also

60 have a weathering-impeding effect (e.g., Lohse and Dietrich, 2005; Navarre-Sitchler et al., 2015; Kim et al., 2017; Gerrits et

61 al., 2021) causing a mitigation of the weathering depth and -intensity. Such mechanisms comprise (1) a forcing process like

62 the formation of secondary minerals and (2) a responsive process such as reduced infiltration of fluids to depth. The latter

63 process damps the initial forcing process of secondary mineral formation, and the mechanism is therefore called negative

64 feedback between (1) and (2).

65 Deciphering the relationship between the formation of secondary minerals and the climatic conditions they were formed under

66 is a prerequisite for understanding the weathering system. It allows to determine whether feedbacks between the formation of

67 secondary minerals and the infiltration of fluids affect the intensity and depth of primary mineral weathering. We hypothesize

68 that a positive feedback loop results in a deep weathering depth, as secondary minerals form fluid pathways by fracturing due

69 to volume increase. On the other hand, we think that a negative feedback loop leads to a shallow weathering depth, as the

70 precipitation of secondary minerals seals fluid pathways.

71 To explore such connections and to elucidate the impact of secondary minerals on the development of weathering systems in

72 different climatic zones, we investigated two 6 m deep weathering profiles in the Chilean Coastal Cordillera. One profile is

73 located in a Mediterranean and another in a humid climate zone, and both developed from weathering of granitic rock. Both

74 sites are eroding and the surfaces in the locations are thus constantly turned over (see compilation of rates and environmental

75 parameters in Oeser and von Blanckenburg (2020) and references therein). The profiles were sampled in soil pits and

76 complemented with rock samples obtained by deep wireline rotary drilling close to the soil pits. Samples were investigated by

77 a combination of analytical techniques such as X-ray fluorescence and micro-X-ray fluorescence as well as oxalate-/dithionite

78 extraction to characterize the geochemical composition, and X-ray diffraction, magnetic susceptibility measurements, electron

79 microprobe as well as light microscopy to identify the mineral assemblages. The combined results of these techniques are used

80 to derive weathering-intensifying and -mitigating processes during subsurface weathering and to elucidate how these processes

81 influence the depth and intensity of weathering in the different climate zones.

82 **2 Study sites**

83 **2.1 La Campana (LC)**

84 The soil pit (-33.02833° N, -71.04370° E, 894 m) and the drilling site some 15 m next to it (-33.02833° N, -71.04354° E,

85 898 m) are located south of the La Campana National Park approximately 60 km NW of Santiago de Chile (Fig. 1a). They are

86 situated on a ridge with steep slope dip angles of 20–30°.

87 The vegetation can be characterized as Mediterranean sclerophyllous forest with *Cryptocarya alba* and *Lithraea caustica* as

88 dominant plants (Luebert and Pliscoff, 2006; Oeser et al., 2018; Fig. 1b,c). The annual precipitation rate (measured from April

89 2016 to April 2020) is 346 mm yr^{-1} (Übernickel et al., 2020) and the Holocene net primary production is 280 ± 50 g$_C$ m^{-2} yr^{-1}

90 (Werner et al., 2018).

91 The regolith profile developed on top of Upper Cretaceous intrusions of mainly granodiorites and tonalites with subordinate

92 quartz monzodiorites (Gana et al., 1996). The depths of the soil horizons are A: 0–30 cm, B: 30–83 cm and C (saprolite): >83

93 cm (Fig. 1d). Uplift rates for the north of Santiago de Chile vary between 0.01 and 0.23 mm yr^{-1} with a general mean value of

94 0.13 ± 0.04 (Melnik, 2016). The soil denudation rate in the nearby La Campana National Park is 53.7 ± 3.4 (S-facing slope)

95 to 69.2 ± 4.6 t km^{-2} yr^{-1} (N-facing slope; Oeser et al., 2018).

2.2 Nahuelbuta (NA)

The investigated soil pit (-37.79371° N, -72.95065° E, 1113 m) and the drilling site next to it (-37.79381° N, -72.95043° E, 1114 m) are located approximately 20 km west of Angol (Region IX (Araucanía), Province Malleco) in southern Chile (Fig. 1a). The borehole was located on a plateau-like ridge with gently dipping slopes (ca. 10°).

The pre-land-use vegetation in the study area resembled the recent vegetation found in the Nahuelbuta National Park which can be characterized as temperate forest with *Araucaria araucana* as the dominant tree (Luebert and Pliscoff, 2006; Fig. 1e). However, extensive modern pastoral farming (cow grazing) and fires have converted the ecosystem in the study area to a sparse forest of deciduous trees such as *Nothofagus obliqua* (see Oeser et al., 2018; Fig. 1f). Numerous signs of burning can be observed in the field and charcoal is an integral component of the soil down to 25 cm (A horizon). The precipitation rate (measured from end of March 2016 to April 2020) is 1927 mm yr^{-1} (Übernickel et al., 2020) and the Holocene net primary production is 520 ± 130 g$_C$ m^{-2}yr^{-1} (Werner et al., 2018).

The regolith profile developed on top of granitoid rocks of the Nahuelbuta central pluton which contains heterogenous lithological portions (Hervé, 1977; Ferraris, 1979). It is part of the Nahuelbuta Batholith which in turn belongs to the late Carboniferous Chilean Coastal Batholith (Steenken et al., 2016; Deckart et al., 2013). The depths of the soil horizons are A: 0–25 cm, B: 25–90 cm, and C (saprolite): >90 cm (Fig. 1g). Today´s exhumation rates in NA are high (>0.2 mm yr^{-1}; Glodny et al., 2008b), whereas the catchment-wide denudation rate is small (27.4 ± 2.4 mm kyr^{-1}; van Dongen et al., 2019) compared to LC. The soil denudation rate in the nearby Nahuelbuta National Park ranges between 17.7 ± 1.1 (N-facing slope) to 47.5 ± 3.0 t km^{-2} yr^{-1} (S-facing slope; Oeser et al., 2018). Tectonic fractures in NA can be related to the Lanalhue Fault Zone (see Glodny et al., 2008a).
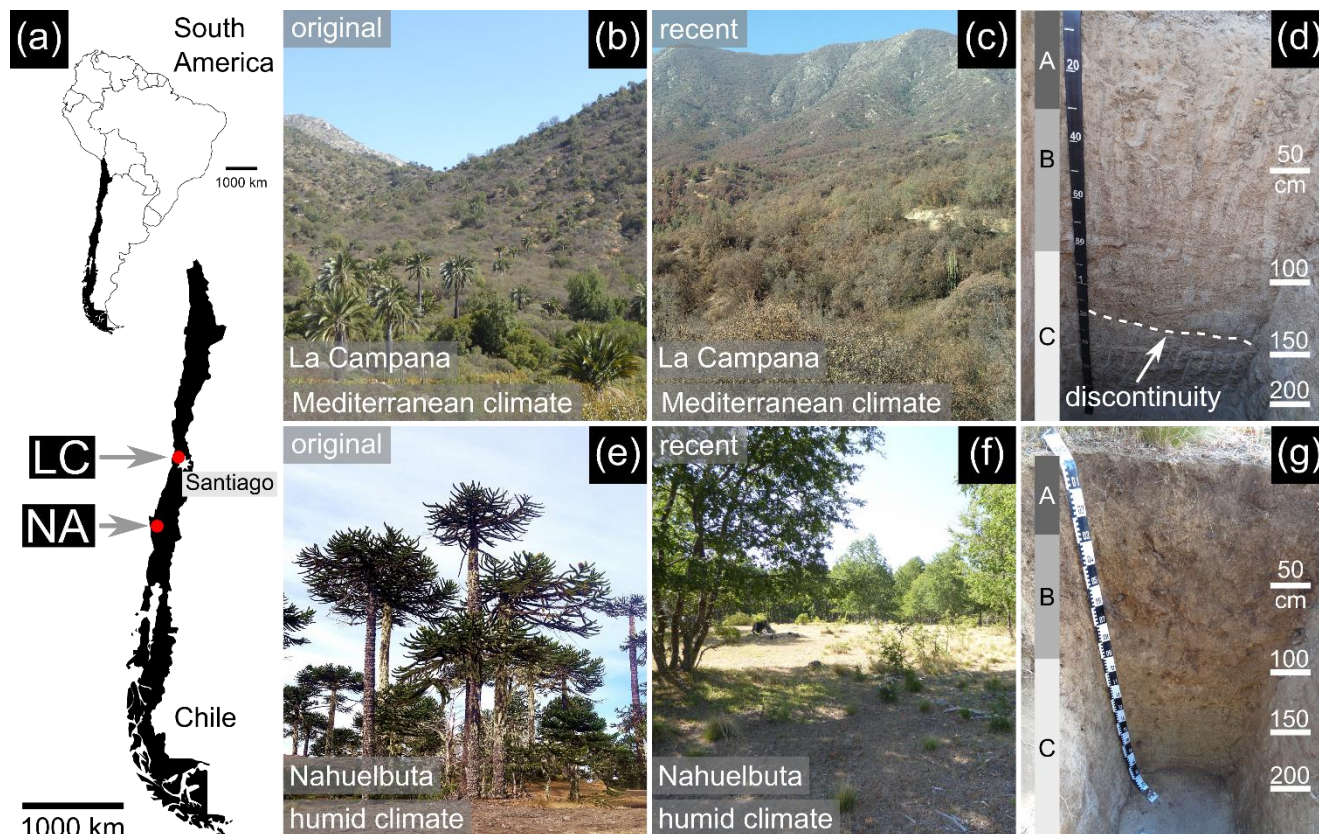
Figure 1: Overview of the study sites and soil profiles. (a) Position of La Campana (LC) and Nahuelbuta (NA) in Chile. Modified map data from **OpenStreetMap** (© **OpenStreetMap** contributors). (b) Original vegetation in LC (i.e., before human intervention; La Campana National Park). (c) Vicinity of the soil pit and drilling site in LC and (d) the first 2 m of the soil profile in LC with inscribed soil horizons (A-C). A prominent discontinuity (dashed line) can be found in the depth interval 120–140 cm. (e) The original vegetation in NA (i.e., before human intervention; Nahuelbuta National Park) in comparison to (f) the recent vegetation in the vicinity of the soil pit and drilling site. (g) The first 2 m of the soil profile in NA with inscribed soil horizons (A-C).

3 Materials and methods

3.1 Soil pit sampling, drilling, and sample preparation

The sampled 6 m deep soil profiles were located close to the main boreholes at the respective sites. Bulk samples were collected in 20 intervals in each soil pit and weighed around 3 kg. Corestones were not encountered in the soil pit profiles of LC and NA. By using a rotary splitter (type PT, Retsch) the bulk samples were separated into aliquots (see Hampl et al., 2022b). During the drilling campaigns, up to 1.5 m long core runs were recovered by wireline diamond drilling (~80 mm core diameter) using potable water as drilling fluid (see Krone et al. (2021) for a detailed description of the drilling technique). Rock samples were separated from the core by mechanical methods (angle grinder, hammer and chisel), cut (diamond saw), impregnated with blue artificial resin filling the porosity, and subsequently thin-sectioned. Representative bedrock samples were separated from the core (diamond saw) and crushed (jaw crusher).

3.2 Analytical methods and calculations

A detailed description of the analytical methods can be found in the accompanying data publication of this study (Hampl et al., 2022b).

3.2.1 X-ray fluorescence (XRF) and micro-X-ray fluorescence (µ-XRF)

Soil pit samples were ground with an agate disc mill and annealed (950°C for 1h) before adding a lithium borate flux to produce glass beads in platinum crucibles. The element composition of the glass beads was analysed with a Thermo Scientific ARL PERFORM'X X-ray fluorescence sequential spectrometer (WD-XRF; Thermo Fisher Scientific Inc., U.S.A.). Additional powder pellets were produced by mixing the ground air-dried samples with wax. The mixtures were pressed and analysed with a SPECTRO XEPOS energy dispersive X-ray fluorescence spectrometer (ED-XRF, SPECTRO Analytical Instruments GmbH, Germany). Polished sample slabs of bedrock (Fig. 2) were mapped for the spatial distribution of elements with a µ-XRF spectrometer M4 Tornado (Bruker, Germany).

Geochemical calculations

Zr contents obtained from the XRF element analyses on powder pellets were used as an immobile element for the calculation of the chemical depletion fraction (CDF; Riebe et al., 2003; Eq. 1), and the mass transfer coefficient (τ; Anderson et al., 2002; Eq. 2).

$$\text{CDF} = 1 - \frac{Zr_N^b \cdot (sum^w - LOI^w)}{Zr_N^w \cdot (sum^b - LOI^b)} , \tag{1}$$

$$\tau = \frac{X^w \cdot Zr^b}{X^b \cdot Zr^w} - 1 , \tag{2}$$

LOI^b = loss on ignition of the bedrock, LOI^w = loss on ignition of the weathered sample, sum^b = measured total sum (wt.%) of the bedrock, sum^w = measured total sum (wt.%) of the weathered sample, X^b = concentration of element X in the bedrock, X^w = concentration of element X in the weathered sample, Zr^b = concentration of Zr in the bedrock, Zr_N^b = zirconium content of the bedrock normalized to a LOI-free sum of 100 %, Zr^w = concentration of Zr in the weathered sample, Zr_N^w = zirconium content of the weathered sample normalized to a LOI-free sum of 100 %.

The chemical index of alteration (CIA; Nesbitt and Young, 1982) was modified to ΔCIA (Eq. 3).

$$\Delta\text{CIA} = \left[\left(\frac{Al_2O_3^w}{Al_2O_3^w + CaO^w + Na_2O^w + K_2O^w} \right) - \left(\frac{Al_2O_3^b}{Al_2O_3^b + CaO^b + Na_2O^b + K_2O^b} \right) \right] \cdot 100 , \tag{3}$$

163   *w = in the weathered sample, b = in the bedrock.*

164

3.2.2 Oxalate- and dithionite extraction

166   Air-dried bulk samples of <2 mm (dry-sieved) were used for oxalate- and dithionite extractions. The solutions thus obtained

167   were measured with an ICP-OES iCAP 6300 DUO (Thermo Fisher Scientific, USA) to determine the extractable Fe, Al, and

168   Si contents. The oxalate extraction employed targets the easily extractable mainly X-ray amorphous Fe(III) oxyhydroxides and

169   (poorly) crystalline Al-containing minerals (see review by Rennert (2019) and references therein). The dithionite extraction

170   dissolves crystalline and amorphous iron oxides (McKeague and Day, 1966). In doing so it can (partly) attack Al-bearing

171   (mineral) phases (see review by Rennert (2019) and references therein).

172   The oxalate extractions were performed after Schwertmann (1964) with an oxalic acid-/oxalate-extraction solution (0.2 M, pH

173   3.0). After the addition of the solution to the sample and shaking for 2 h in the dark (over-head shaker), the solution was filtered

174   in a darkened room and immediately measured. The cold dithionite extractions were performed based on Holmgren (1967)

175   with an extraction solution (mixture of 0.2 M $NaHCO_3$ and 0.24 M trisodium citrate) and sodium dithionite under oxic

176   conditions. The resulting mixture of chemicals and sample was shaken for 16 h and centrifuged before the supernatant was

177   filtered and immediately measured. Additional reference samples, blanks and calibration solutions were also prepared and

178   measured like the soil pit samples. The results of the samples presented here are the mean of duplicate measurements performed

179   on two individually extracted sample aliquots.

3.2.3 Grain size determination

181   Sample aliquots were suspended in de-ionized water (<10 μS m^{-1}) and dispersed in a rotating overhead shaker (approx. 15 h)

182   and a subsequent ultrasonic bath before vibrational wet sieving. The >63 μm sieving fractions were dried (50°C, approx. 24

183   h) and their weight percentages were measured. The clay and silt contents were determined using the <63 μm suspension and

184   a pipette method. Organic-rich samples were treated with H_2O_2 to decompose organic matter and sodium pyrophosphate was

185   used as a dispersion agent to prevent coagulation. Clay (<2 μm) was separated from the <63 μm fraction slurry via

186   centrifugation.

3.2.4 X-ray diffraction (XRD)

188   Untreated air-dried aliquots of bulk samples were crushed in a porcelain mortar and afterwards processed with a micronisation

189   XRD-mill McCrone (Retsch, Germany) to obtain a final powder of <10 μm. These powders were mounted to XRD sample

190   holders by back-loading and X-ray diffraction measurements were performed with a Rigaku SmartLab equipped with a 9 kW

191   rotating Cu-anode and a HyPix-3000 detector in Bragg-Brentano geometry (3–80° 2θ, scan step: 0.01°, scan speed: 1° min^{-1},

192   and 60 rpm sample rotation). For the identification and semi-quantitative analyses, the software SmartLab Studio II and the

193   mineral database PDF-4 Minerals 2021 including reference intensity ratio (RIR) factors were used. Image processing (imageJ;

194 version 1.53a; Schneider et al., 2012) performed on the µ-XRF element distribution maps in Fig. 2 was used to get a rough

195 compositional information of the mineral content in the sampled bedrock. These analyses were used as a supporting basis for

196 the semi-quantitative XRD analyses with RIR factors.

197 Clay mineral contents in the samples were quantitatively estimated by combining the results of the grain size determination

198 with the semi-quantitative results of the XRD analyses. The clay-size fraction (<2 µm) of which the mass was determined by

199 sieving/pipetting, was assumed to represent the entire clay mineral content of the sample, while the other size fractions were

200 considered to be free of clay minerals. This assumed clay mineral content (in wt.%) was combined with the XRD-semi-

201 quantitative weight percentages of the primary minerals in the same sample to approximate the mineral composition of the

202 whole soil pit sample (summarized to 100 wt.%). Despite the assumption that only the <2 µm grain size fraction contains clay

203 minerals, this estimate appears to be the most accurate because there are no matching files in the mineral database used here

204 that would accurately semi-quantify the identified interstratified clay minerals.

205 The separated clay-size fractions were measured as oriented clay films (texture preparation). A D2 Phaser XRD device

206 (Bruker) equipped with a Cu-anode was utilized for the measurements. The diffractograms were recorded in Bragg-Brentano

207 geometry in the range of 3–35° 2θ (step width: 0.01° 2θ, 0.5 seconds per step). The samples were measured after air-drying,

208 during ethylene glycol saturation and after a thermal treatment at 550°C for 1 h. Selected samples were also treated with

209 glycerol and KCl (1 M) to characterize the clay minerals in more detail. The identification was supported by a clay mineral

210 identification chart (Starkey et al., 1984).

211 **3.2.5 Magnetic susceptibility measurements**

212 The magnetic susceptibility was measured on all twenty-one McCrone-milled bulk samples of the LC profile with a KLY-3

213 Kappabridge (AGICO, Czechia). Measurements were performed in triplicates at room temperature, a frequency of 875 Hz and

214 a peak magnetic field of 300 A m^{-1}.

215 To obtain the magnetite content of the bedrock, a representative 60x60 mm sample slab (Fig. 2a) was mapped with the µ-XRF

216 spectrometer M4 Tornado. The µ-XRF map that depicts only the maximum Fe content was used as an approximation of the

217 magnetite content since magnetite is the mineral with the highest Fe concentration in the rock. Finally, the map was analysed

218 with the image processing program imageJ (version 1.53a; Schneider et al., 2012) to quantify the magnetite content. The

219 obtained value was equalled to the measured magnetic susceptibility of the same sample and used to convert the magnetic

220 susceptibility results of the LC soil pit samples into approximated magnetite contents by the rule of three. The investigated

221 bedrock of NA contains no magnetite.

222 **3.2.6 Light microscopy and electron microprobe analysis (EMPA)**

223 Thin sections were investigated with the light microscope DM750P (Leica, Wetzlar, Germany) equipped with a microscope

224 camera (Euromex, The Netherlands). Electron microprobe element distribution maps of selected areas were obtained for Al,

Earth **Surface**
Dynamics
Discussions

225 Ca, Fe, K, and Mg by using standard wavelength dispersive techniques on a JEOL Superprobe JXA-8230 fitted with a W-

226 emitter electron gun (accelerating voltage: 15 kV, beam current: 20 nA, beam diameter and step width: 1 µm).

227 **4 Results**

228 The data tables (cited as Table S1–S5) are included in the accompanying data publication (Hampl et al., 2022b).

229 **4.1 Bedrock**

230 According to the Streckeisen nomenclature the bedrock of LC can be described as granodiorite and the investigated bedrock

231 of NA can be described as granite. However, the drill core revealed that the bedrock of NA occasionally contains more mafic

232 sections. The most abundant minerals in the fine-grained bedrock of LC are plagioclase, quartz, microcline, hornblende, biotite,

233 and chlorite (Fig. 2a,b). The latter occurs solely and abundantly along with (former) biotite crystals as their hydrothermal

234 transformation products (i.e., chloritization; e.g., Kogure and Banfield, 2000). Magnetite is a ubiquitous accessory mineral

235 (Fig. 2c; <1 vol.%) in LC and shows no signs of alteration to hematite (martitisation). Pyrite and chalcopyrite are also observed

236 in much smaller abundance than magnetite. Mafic xenoliths can frequently be found in the granodiorite of LC.

237 In the coarse-grained Nahuelbuta granite, quartz, plagioclase, microcline, biotite, and chlorite are the main constituents (Fig.

238 2d,e). In contrast to LC, amphiboles can only be found as an accessory mineral (<1 vol.%) in the investigated bedrock of NA.

239 Like in LC, biotite is often chloritized. Magnetite and sulfides could not be identified in the investigated rock samples of NA.

240 Variations in the biotite content, the occurrence of amphibole crystals, differences in fabric (microcline of a few centimetres),

241 the alternation with mafic portions and the presence of pegmatites in the core make the overall lithology of NA far more

242 heterogenous compared to LC.

243

Earth **Surface**
Dynamics
Discussions
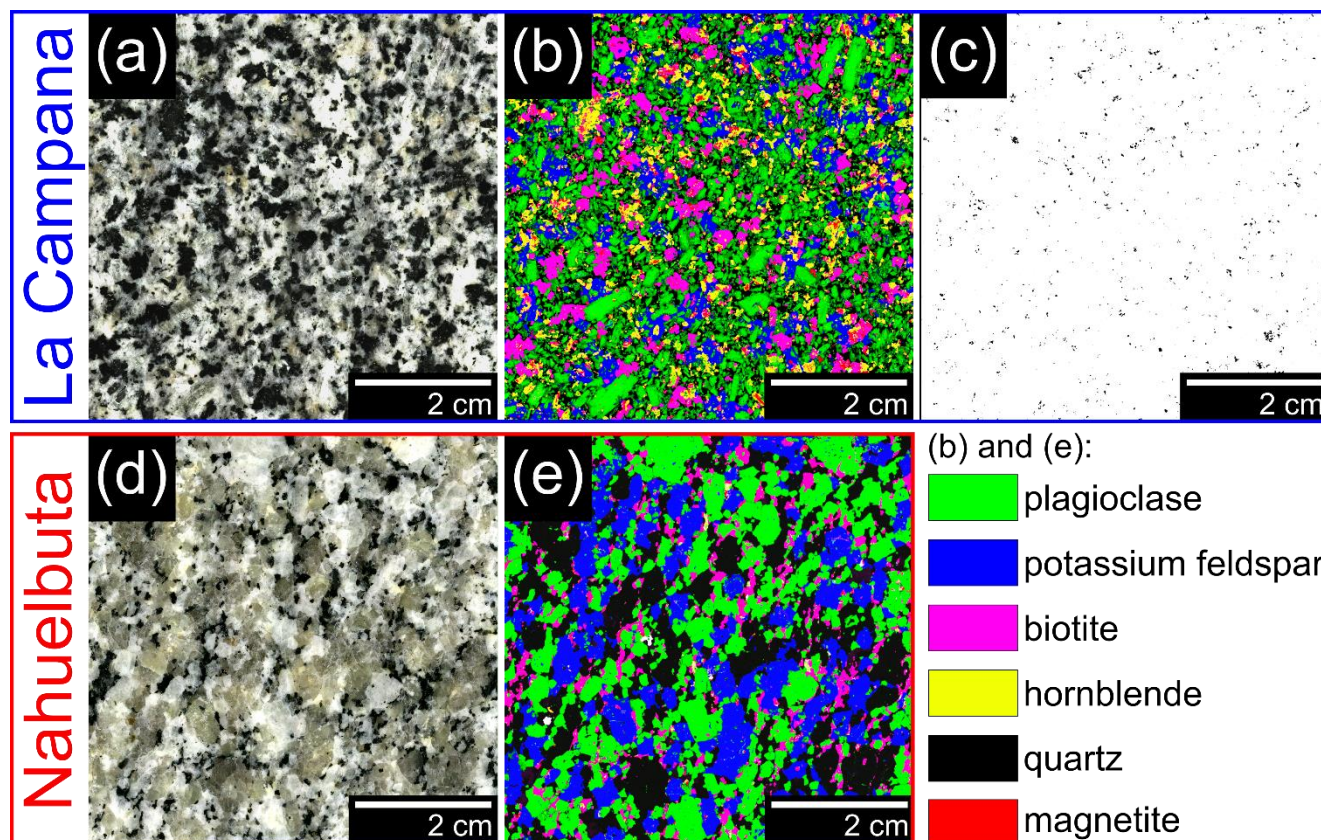
Figure 2: Bedrock of the investigated profiles. (a) Bedrock from La Campana (IGSN: GFFJH0095) with (b) a corresponding µ-XRF map reflecting the spatial mineral distribution. (c) µ-XRF map of the maximum Fe content (black dots) representing the magnetite crystals in the bedrock sample slab of La Campana. (d) Typical unweathered granite from Nahuelbuta (IGSN: GFFJH00H0) and (e) a µ-XRF map reflecting the mineral content of the same.

4.2 Regolith

4.2.1 Incipient weathering in rock

Weathered rock from the borehole of LC shows abundant indications of weathering-induced fracturing (WIF) due to Fe(II) oxidation in biotite, like fanned-out edges or opening due to dilatation (Fig. 3a,b). Secondary minerals like Fe(III) oxyhydroxides are subordinate and are mostly associated with biotite. They are detectable as Fe-enrichments at the edge of biotite crystals and within the cracks encompassing biotite (Fig. 3c,d). To a minor degree, Fe(III) oxyhydroxides are also associated with hornblende. Nevertheless, most micro-fractures in feldspar and quartz of the investigated thin sections are solely filled with blue resin and are bare of any secondary minerals.

Earth **Surface**
Dynamics
Discussions
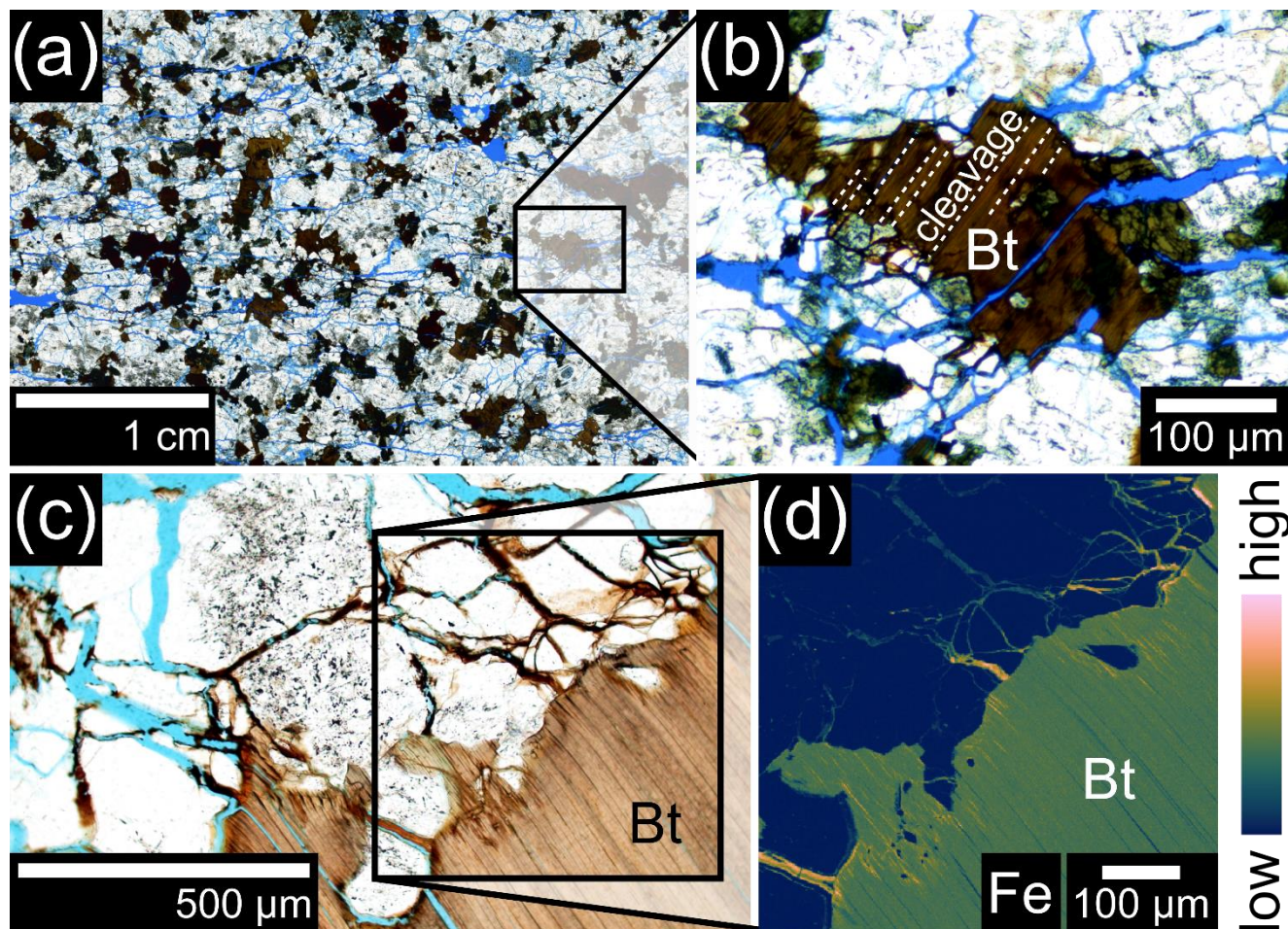
Figure 3: Rock weathering in La Campana (LC; porosity is represented by blue-dyed resin). (a) Thin section image (transmitted light) of a weathered rock sample obtained from approx. 27 m depth in the LC drill core (IGSN: GFFJH00HY). (b) A detail image of biotite showing signs of dilatation (dashed lines indicate cleavage planes). (c) Secondary minerals in cracks around biotite. (d) The electron microprobe map of the contact zone between biotite and quartz/feldspar displays Fe-enrichments at the interface. Bt = biotite.

Indications of WIF around biotite are also present in weathered rock of NA (Fig. 4a,b). However, the cracks are often filled and covered with Fe(III) oxyhydroxides and clay minerals as observed with light microscopy (Fig. 4c) and electron microprobe investigations. Unlike LC, weathered rock in NA is characterized by distinct Ca-depletion and Al-enrichment in plagioclase which indicates partial dissolution (Fig. 4d–f). These alteration sites host secondary minerals covering the newly formed surfaces which were formed by the dissolution of the plagioclase.

Earth **Surface** Dynamics
Discussions
Open Access
EGU
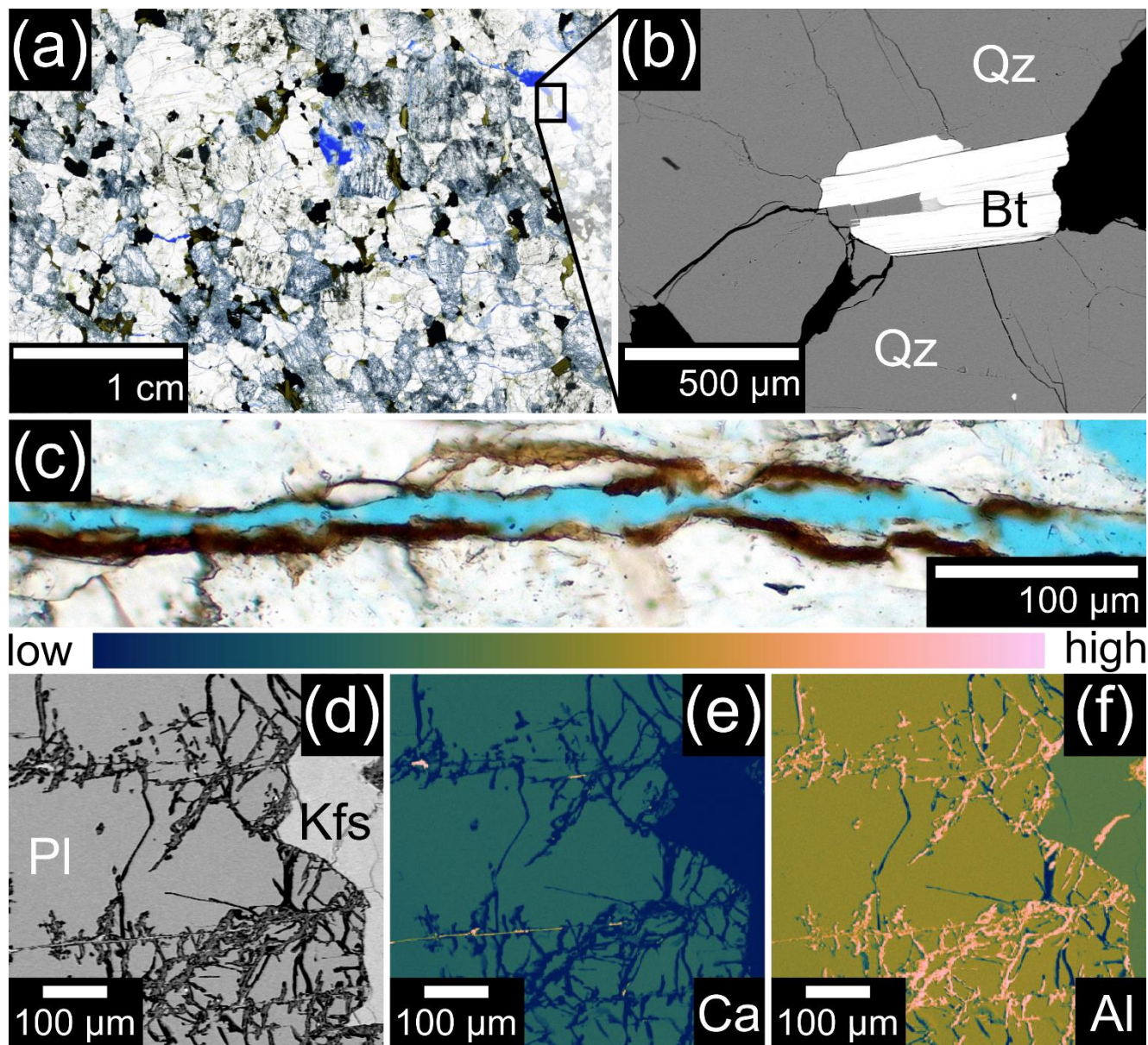
Figure 4: Rock weathering in Nahuelbuta (NA). (a) Thin section image (transmitted light) of weathered rock obtained from approx. 6 m depth in the NA drill core (note that the porosity (blue) is largely associated with weathered plagioclase; IGSN: GFFJH00HX). (b) Indications of WIF in quartz (backscattered electron image, EMP). (c) Thin section image (transmitted light) of a crack covered with brown Fe(III) oxyhydroxides from approx. 12 m depth (IGSN: GFFJH00J2). (d) Backscattered electron image (EMP) of partly dissolved plagioclase and (e) the respective Ca and (f) Al map of the section (IGSN: GFFJH00HX). Qz = quartz, Bt = biotite, Pl = plagioclase, Kfs = potassium feldspar.

4.2.2 Saprolite and soil

Chemical alteration

The mass transfer coefficient τ indicates moderate depletion below 80 cm (not smaller than -0.2) in the LC soil pit profile, but clear depletion in the uppermost few decimetres where Na, K, Mg, Ca, Si and P can reach up to $\tau = $ -0.5 and -0.6 (Fig. 5; Table S1). A pronounced P depletion can be detected down to 1.4 m depth in LC. The chemical depletion fraction (CDF) of LC and the bedrock-normalized chemical index of alteration (ΔCIA) indicate a weak chemical weathering degree below ca. 0.5–1 m, but minor chemical depletion was analysed down to the bottom of the 6 m deep profile of LC (see ΔCIA; Fig. 5).

In contrast, Nahuelbuta is characterized by distinct chemical depletion of Ca and Na (up to $\tau = $ -0.9; Fig. 5). K is depleted to a depth of approximately 5 m, Si to a depth of ~6 m and Mg shows moderate depletion ($\tau \geq $ -0.3) throughout the profile. P is strongly depleted between ca. 2–6 m ($\tau \sim$ -0.6) but the P content gradually increases from approx. 3 m depth towards the surface and is enriched in the uppermost ~20 cm of the soil (A horizon; Fig. 5). The CDF values of NA indicate depletion down to the bottom of the profile at 6 m depth. The ΔCIA of the profile underpins strong chemical alteration compared to the bedrock (Fig. 5). However, overall chemical depletion decreases towards the bottom of the soil profile and according to the τ-values in 550–600 cm only Na, Ca and P seem to be significantly depleted at >6 m depth.
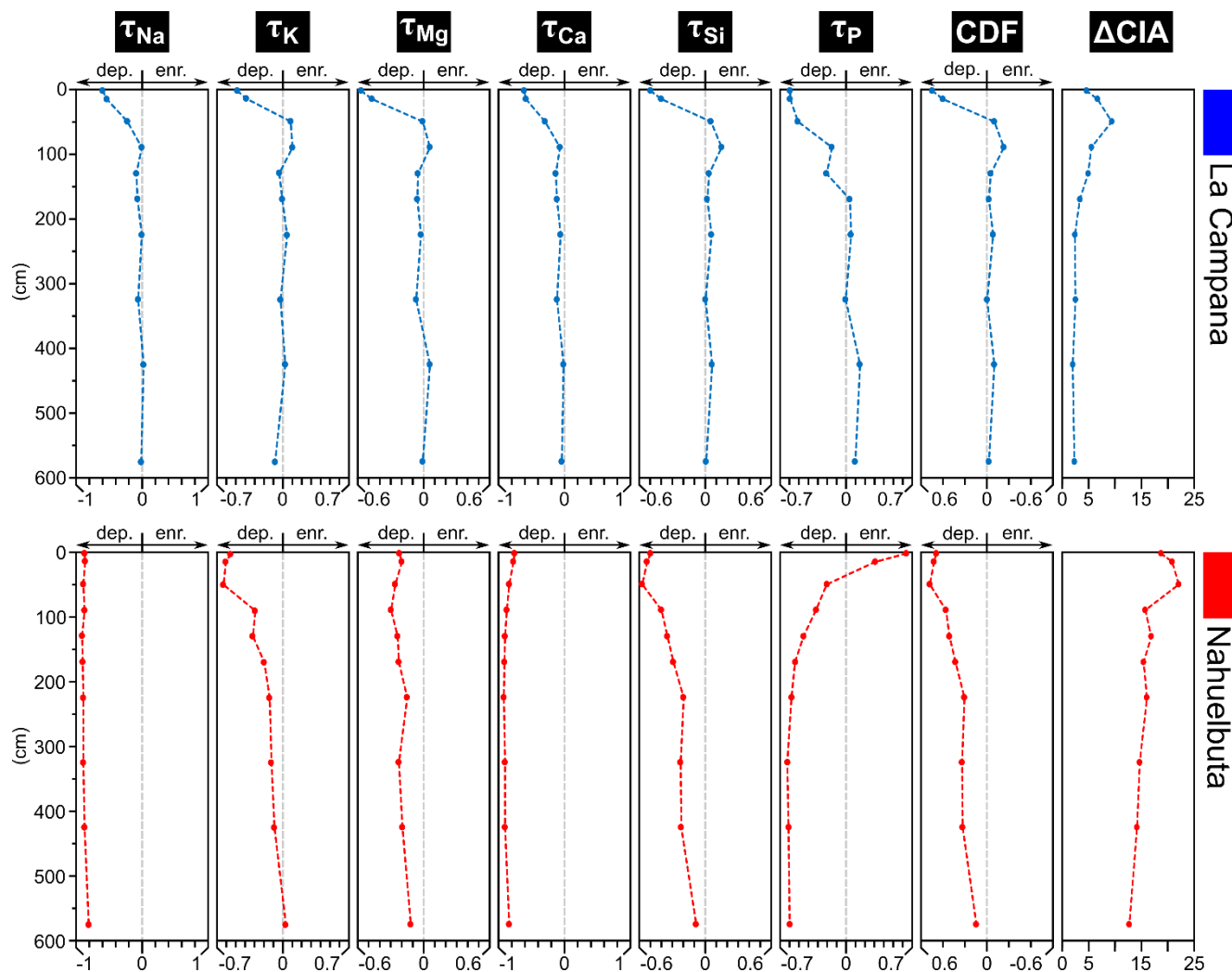
Figure 5: τ-values of Na, K, Mg, Ca, Si, and P as well as the CDF (all based on Zr) and ΔCIA values of the soil pit profiles in La Campana (LC) and Nahuelbuta (NA; Table S1). Note that the scales are equal for the individual indices of LC and NA. dep. = depletion, enr. = enrichment.

Since many secondary minerals are formed via a metastable or amorphous precursor (e.g., Steefel and van Cappellen, 1990; Hellmann et al., 2012; Behrens et al., 2021), we assume that the extractable Fe, Si, and Al contents are indicative for recent weathering of primary minerals (Fig. 6; see chapter 3.2.2 for an assignment of the extractable elements to the minerals they likely originate from).

Earth **Surface**
Dynamics
Discussions
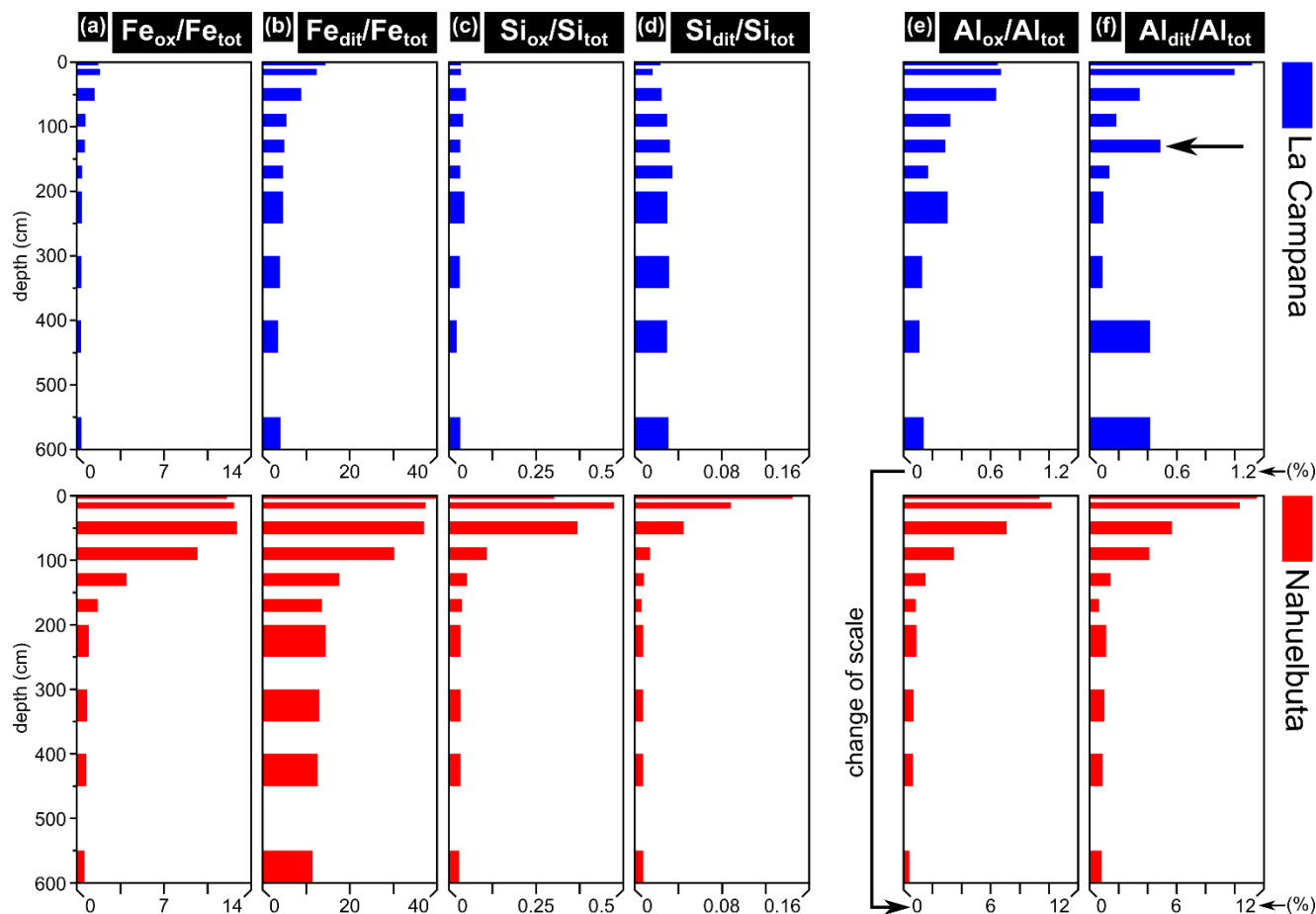
Figure 6: Oxalate- and dithionite-extractable Fe, Si and Al contents divided by the respective total element contents of the bulk soil pit samples of La Campana (LC) and Nahuelbuta (NA; Table S2). The elevated ratio at 120–140 cm in (f) (arrow) coincides with the position of a discontinuity in the profile (Fig. 1d). Note that the scales for LC and NA are equal in (a)–(d). The scale in (e) and (f) is one order of magnitude larger for NA compared to LC.

Extractable contents of Fe in LC are moderately elevated in the uppermost meter of the profile (up to Fe_{dit}/Fe_{tot} ~14 %) compared to the other depth intervals which show low contents (Fe_{dit}/Fe_{tot} <1 m: ~4–5 %; Table S2; Fig. 6a,b). The extractable Si-contents show no clear pattern (Fig. 6c,d) whereas oxalate-/dithionite-extractable Al-contents are variable in the profile of LC (Fig. 6e,f). The elevated Al_{did}/Al_{tot} value in the depth interval 120–140 cm in LC (~0.5 %; Fig. 6f) coincides with a discontinuity in the saprolite (Fig. 1d) and may indicate more secondary crystalline and amorphous Al-bearing phases in this section. The profile in NA is characterized by high amounts of extractable Fe, Si and Al contents which are especially elevated in the uppermost meter of the profile (Fe_{dit}/Fe_{tot} up to ~40 %, Si_{dit}/Si_{tot} up to ~0.14 %, Al_{dit}/Al_{tot} up to ~12 %). The extractable contents rapidly decrease from the surface towards the bottom of the NA profile and starting at approx. 2 m they are similar down to 6 m (Fig. 6).

316 The Fe_2O_3 content in the investigated bedrock of LC is more than twice as high as that of the NA bedrock, but the oxalate- and

317 dithionite-extractable Fe contents (and hence the amount of the respective secondary minerals) are far higher in NA (Fig. 6a,b).

318 The difference between LC and NA is even more pronounced for the extractable Al contents as values in NA can be 10 times

319 higher than in LC (Fig. 6e,f). The extractable contents in the profiles of both study sites are generally within the range of

320 previous investigations on soil samples from the La Campana and Nahuelbuta National Parks, but the Fe_{dit}/Fe_{tot} contents in the

321 upper profile section of NA in this study are much higher (up to 40 %) than those measured in the Nahuelbuta National Park

322 (<25 %; Oeser et al., 2018).

323

Mineral content and grain sizes

325

326 The sieving results of LC show a gradual decrease in particle size from the bottom of the profile towards the surface and a

327 relatively constant sand-size content ranging from 65–80 wt.% with similar portions of the individual sand-size fractions (Fig.

328 7a). The small geochemical depletion below the uppermost ~2 m of the LC profile (Fig. 5) is also reflected in the little changing

329 mineral composition of the profile (Fig. 7b). Only the plagioclase (Ca-albite) content slightly decreases from approx. 1 m depth

330 towards the surface. A small decrease of biotite in the depth interval 120–140 cm coincides with the mentioned discontinuity

331 of this profile section (Fig. 1d). The abundant chlorite of the investigated bedrock in LC (~5 wt.%) is completely weathered

332 and absent from the soil pit samples (Fig. 7b).

333 Significant alteration of magnetite (e.g., martitisation) could not be observed in ore microscopic investigations of the magnetic

334 particles in soil pit samples of LC. Thus, the magnetic susceptibility directly reflects the magnetite content of the samples (e.g.,

335 Ferré et al., 2012). A relative magnetite enrichment was detected in the uppermost 40 cm of the LC profile (1–1.6 %) whereas

336 the rest of the profile shows approximately constant magnetite contents (mean ~0.9 %) close to the value of the investigated

337 bedrock (0.94 %; Fig. 7c). This almost consistent magnetite content underlines the homogeneity of the bedrock that was

338 weathered in the 6 m deep soil pit (i.e., no mafic dykes, pegmatites, or major xenoliths).

339 The soil pit profile of NA is characterized by a much higher pebble- and silt/clay-size content compared to LC (Fig. 7d). This

340 reflects the more heterogeneous grain size distribution of the investigated bedrock in NA compared to the bedrock of LC (see

341 Fig. 2). High clay contents can be detected in the uppermost meter of the NA profile (partly >20 wt.%) and the identified

342 mineral content of the soil pit samples differs significantly from the mineral content of the investigated bedrock (Fig. 7e). The

343 plagioclase (Ca-albite) content distinctly decreases from the bottom of the profile towards the surface and the bedrock content

344 of ~28 wt.% partly decreases down to 1 wt.% in the soil pit. The microcline content on the other hand is relatively uniform.

345 Just as in LC, the chlorite of the bedrock analysed here (~1 wt.%) is completely weathered in the NA soil pit profile and is

346 absent from the samples.

347
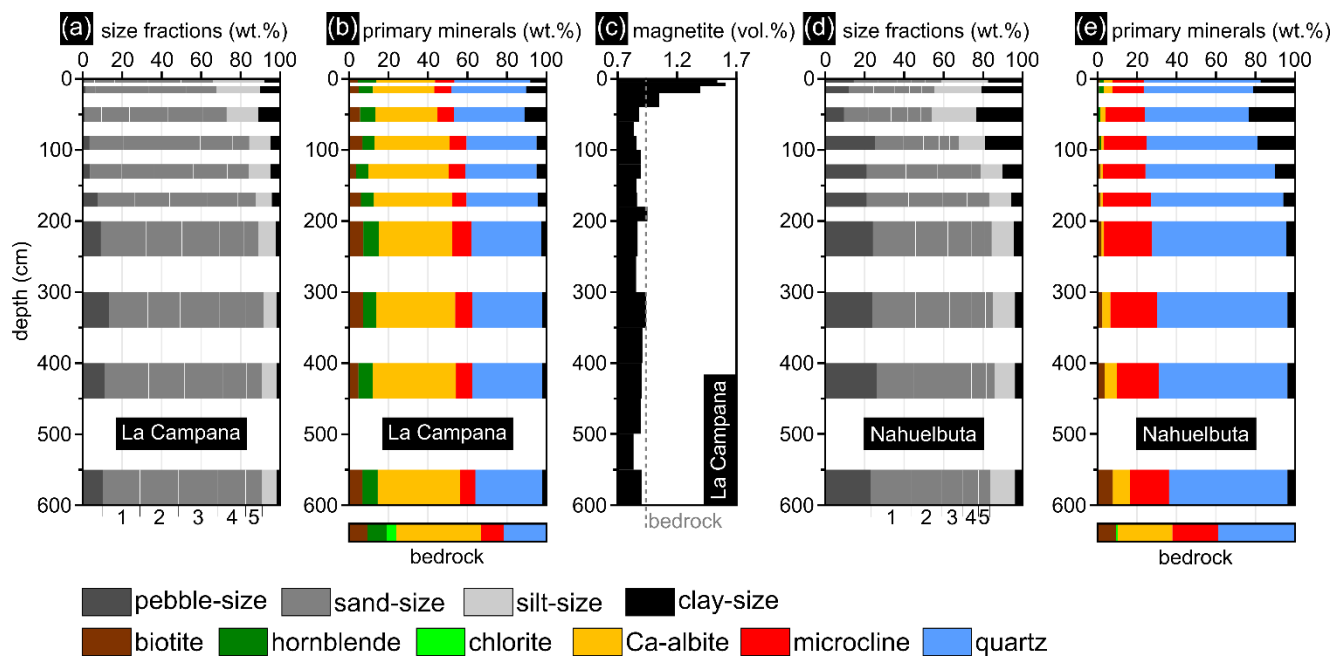
Figure 7: Sieving/pipetting results, semi-quantitative XRD results and approximated magnetite contents of the investigated soil pit samples in La Campana (LC) and Nahuelbuta (NA). (a) Grain size distribution based on wet-sieving and pipetting, (b) semi-quantitative XRD and (c) magnetic susceptibility results converted to approximate magnetite contents of the LC profile. (d) Wet-sieving combined with pipetting results and (e) semi-quantitative XRD results of the NA samples. Semi-quantitative XRD results of the investigated bedrock samples (see Fig. 2) are given below the results of the soil pit samples. In (a) and (d): 1: ≤2000 to >1000 μm, 2: ≤1000 to >500 μm, 3: ≤500 to >250 μm, 4: ≤250 to >125 μm, 5: ≤125 to >63 μm.

The mineral content of the clay-size fraction in LC differs significantly from that in NA (Fig. 8). La Campana is characterized by abundant expandable clay minerals (interstratified chlorite-smectite and interstratified mica-smectite) which can largely be traced back to the weathering of chlorite and biotite (Fig. 8a). Kaolinite can be found throughout the LC profile whereas interstratified mica-vermiculite only occurs in the depth interval of the discontinuity (120–140 cm; see Fig. 1d). The expandable portion of the interstratified minerals gradually decreases from the profile bottom towards the surface and cannot be detected in the uppermost centimetres of the LC profile. Only mica and kaolinite constitute the clay-size fraction of the uppermost part of the profile in LC. The mineral content in the clay-size fraction of NA is characterized by small amounts of interstratified mica-vermiculite below 1 m depth and ubiquitous kaolinite which shows small expandable portions below 2 m depth. Hydroxy-interlayered vermiculite (HIV) and gibbsite can first be detected in 400–450 cm depth and the content increases towards the surface. The main minerals of the clay-size fraction in the uppermost part of the profile are HIV, kaolinite, and gibbsite (Fig. 8b).
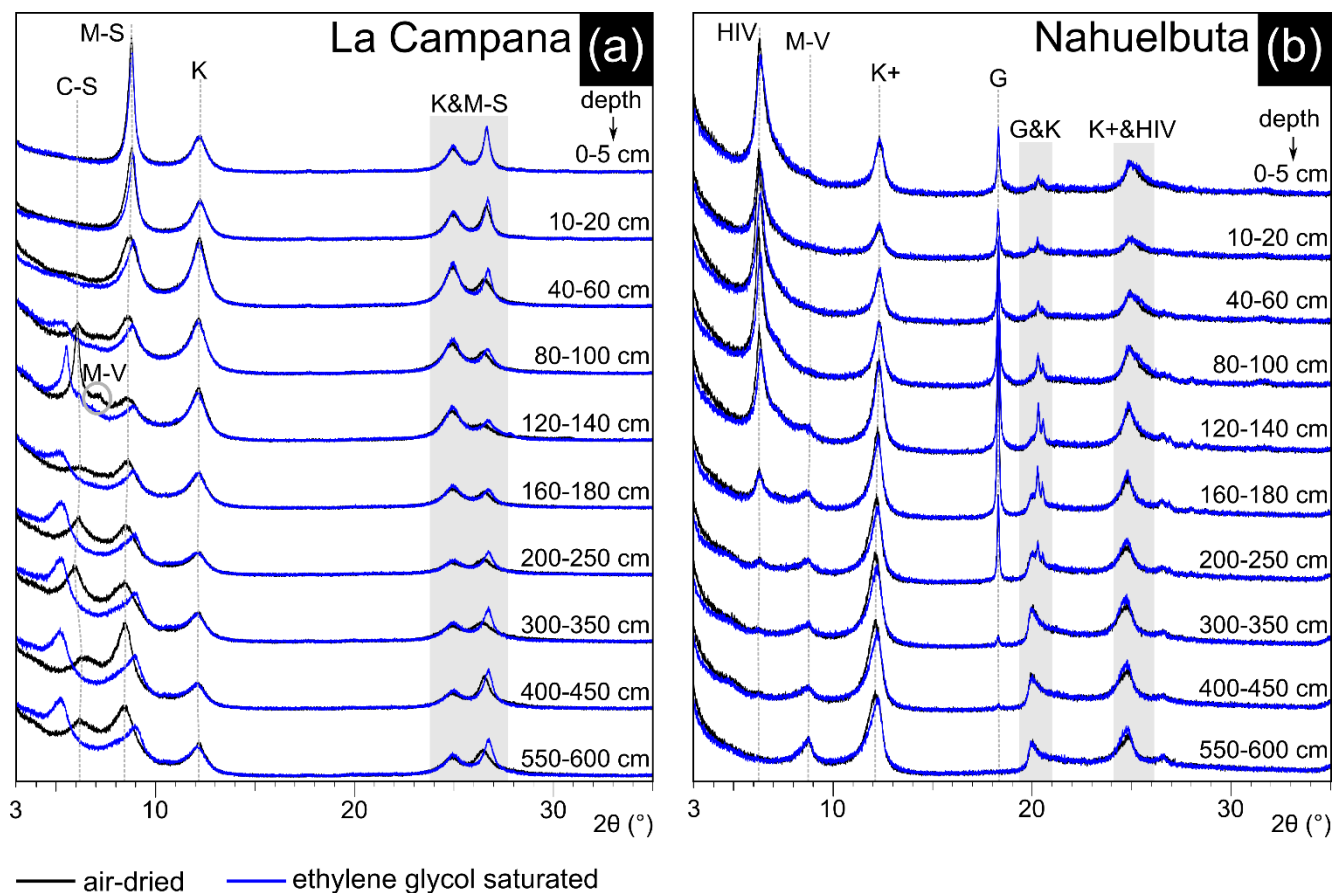
17

Figure 8: Minerals in the clay-size fraction of the soil pit profiles in La Campana (LC) and Nahuelbuta (NA). (a) The profile in LC features abundant expandable clay minerals. (b) NA is characterized by the presence of gibbsite and vermiculite but very minor amounts of expandable clay minerals. C-S = interstratified chlorite-smectite, G = gibbsite, HIV = hydroxy-interlayered vermiculite, K = kaolinite, K+ = kaolinite with expandable portions, M-S = interstratified mica-smectite, M-V = interstratified mica-vermiculite.

5 Discussion

5.1 Climate-dependent mineral transformations

Chemical depletion and mineral transformations are far more pronounced in the profile of NA compared to the profile of LC even though the bedrock of LC contains more minerals with higher solubility compared to NA (more plagioclase, biotite, chlorite or hornblende in LC than in NA where quartz and potassium feldspar dominate; see e.g., Wilson, 2004; Bandstra et al., 2008). The high chemical depletion (τ[Na, Ca] up to -0.9 and ΔCIA up to 22; Fig. 5) and the occurrence of gibbsite in NA are indicative of distinct dissolution of primary minerals (esp. plagioclase; Fig. 7e) and solute removal of alkali and alkaline earth metals while immobile Al remains as hydroxide (Al(OH) = gibbsite). This depletion is assumed to be the result of more water infiltration into the subsurface of NA (more precipitation due to humid climate) compared to LC (less precipitation due to Mediterranean climate). The measured τ[P] distribution in NA is a clear indication for biologically controlled nutrient uplift

381 and recycling within the topsoil (Jobbágy and Jackson, 2004). Thus, we concur with the hypothesis that the ecosystem in NA

382 is thriving on nutrient recycling rather than on an uptake of nutrients that were released by biogenic weathering at depth (Oeser

383 and von Blanckenburg, 2020). Apart from Ca, Na, and P (τ-values in Fig. 5), the chemical depletion successively decreases

384 from the surface towards the bottom part of the investigated profile in NA. To account for this shallow chemical depletion, we

385 propose that a secondary-mineral-controlled impeding of the fluid infiltration to depth is playing an important role for the

386 depth of mineral transformations in NA.

387 Chemical depletion can be detected throughout the investigated profile in LC, but the chemical weathering degree is very low

388 between 2–6 m depth (Fig. 5) and the mineral transformations in this section of the profile are only minor (Fig. 7b). On the

389 other hand, distinct mineral dissolution and removal of solutes is testified by the higher magnetic susceptibility values in the

390 uppermost decimetres of the LC profile. This can be related to a residual accumulation of weathering-resistant magnetite while

391 other minerals like plagioclase dissolve. The strong chemical depletion in this part of the profile is also reflected by the low τ-

392 and elevated CDF-/ΔCIA-values. To account for the detected weak but deep chemical weathering in LC, we propose that a

393 secondary-mineral-controlled formation of fluid pathways is facilitating the fluid infiltration to depth and is thus an important

394 control on the chemical weathering reactions in the subsurface.

395 The difference between the profiles is also displayed by the oxalate- and dithionite-extractable Fe, Si, and Al contents. While

396 high extractable contents especially within the uppermost 2 m of the NA profile are interpreted to indicate considerable

397 ongoing (recent) transformations of primary to secondary minerals, LC shows comparatively little indications in this regard.

398 This difference underlines the higher degree of mineral transformations in NA compared to LC which is also reflected in the

399 mineral content of the clay-size fraction (see Fig. 9). That oxalate- frequently exceeds dithionite-extractable Al contents is

400 indicative for amorphous phases since oxalate is more effective at extracting amorphous forms of Al (McKeague and Day,

401 1966). Moreover, the highest contents of the clay-size fraction in the profiles are in good correlation with the elevated

402 extractable Fe, Si and Al contents and highlight the pronounced mineral transformation in the uppermost part of the profiles.

403 This size fraction hosts most of the products of primary silicate weathering. Clay-size minerals of NA mainly correspond to

404 distinct weathering of plagioclase and biotite, whereas in LC they can mainly be associated with chlorite and biotite weathering

405 (Fig. 9). Feldspar weathers to kaolinite and gibbsite in NA and biotite weathers to hydroxy-interlayered vermiculite (HIV).

406 Chlorite completely dissolved in the NA profile, whereas both chlorite and biotite in LC weather via interstratified clay

407 minerals to smectite. Finally, smectite and feldspar likely weather to kaolinite in LC (Fig. 9).

408
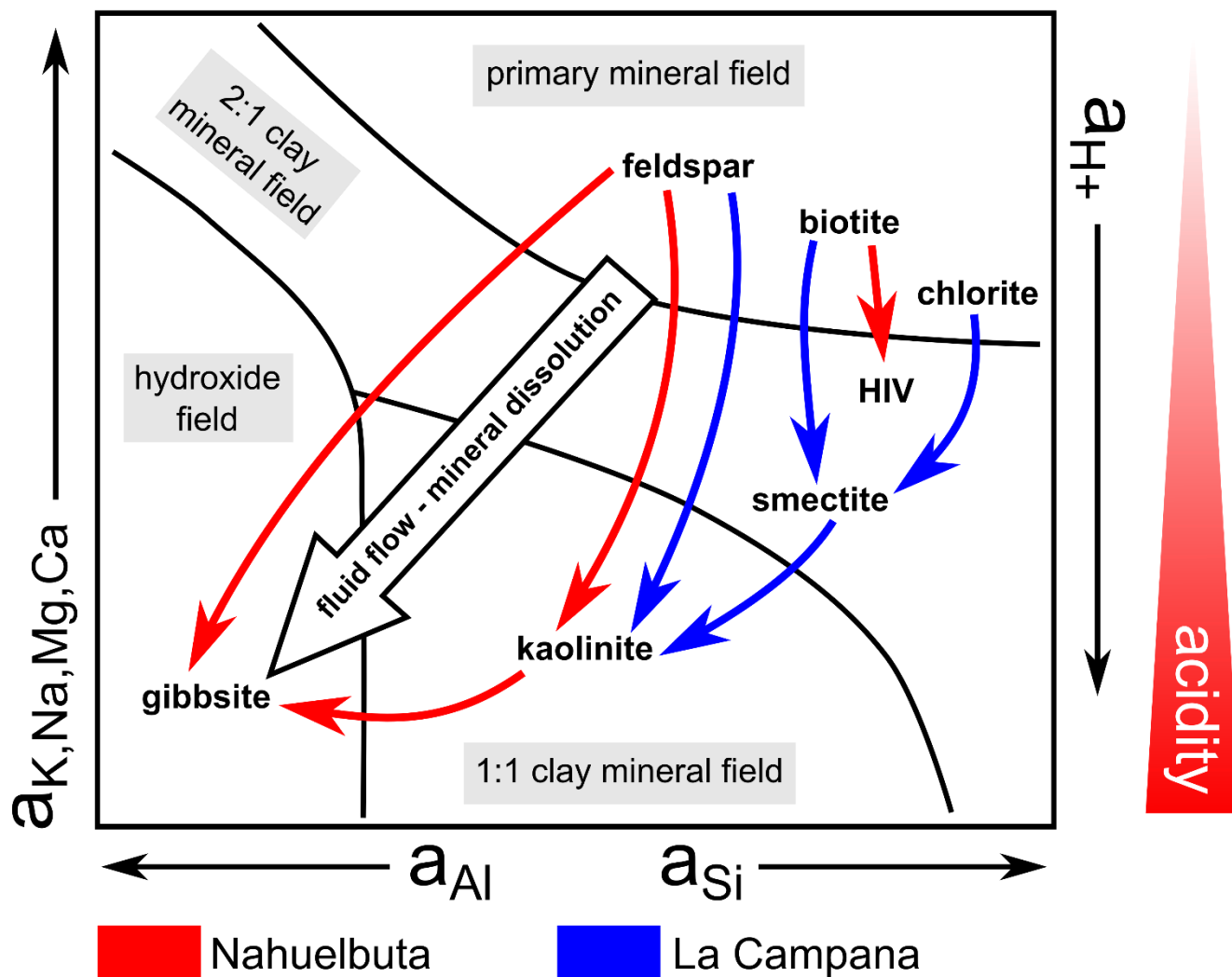
Figure 9: Schematic phase diagram showing the transformation of primary minerals to secondary minerals (clay minerals and
aluminium hydroxide) depending on the activities of H+, Si, Al, K, Na, Mg and Ca. The depletion of the alkali and alkaline earth
metals, and the increase of the Al activity are coupled to an increase of the mineral dissolution and the removal of solutes by a higher
subsurface fluid flow. Elevated a_{H+}-values (i.e., lower pH) increase the mineral solubility. Modified from Chesworth et al. **(2008).**
HIV = hydroxy-interlayered vermiculite, a = thermodynamic activity

5.2 Weathering-intensifying processes

5.2.1 Porosity increase by weathering-induced fracturing and its impact on the weathering depth

Ferrous primary minerals of the LC granodiorite can frequently be identified as initiating locations of micro-cracks. This

observation can be related to weathering-induced fracturing (WIF) due to the increase in volume caused by the oxidation of

Fe(II) in Fe(II)-bearing silicates (e.g., Buss et al., 2008; Behrens et al., 2015; Kim et al., 2017) and the formation of secondary

420   Fe(III) oxyhydroxides (Fletcher et al., 2006; Lebedeva et al., 2007; Anovitz et al., 2021; Fig. 3d). This process generates and

421   increases surface areas of primary minerals and in turn accelerates weathering reactions (positive feedback between the

422   formation of secondary minerals and the infiltration of fluids (esp. O_2 and water) to depth; e.g., Røyne et al., 2008). These

423   weathering-induced fractures consequently facilitate the presence of surface-derived O_2 in the deep subsurface (Kim et al.,

424   2017) and the corresponding transport through the saprolite/soil is dominated by advection (Lebedeva et al., 2007). The

425   bedrock of LC is richer in Fe-bearing minerals than the investigated granite of NA (ca. 25 wt.% in LC and ca. 10 wt.% in NA)

426   and hosts biotite, hornblende, chlorite, and magnetite as Fe(II) sources. A considerable amount of the total Fe content is bound

427   in magnetite (roughly 0.7 wt.% of the total Fe_2O_3 content if the magnetite content of the bulk sample is 1 wt.%). However, we

428   found no microscopic evidence (no oxidation) nor indications in the magnetic susceptibility results that the Fe(II) in magnetite

429   is available for weathering reactions. Thus, we conclude that magnetite is stable under the environmental conditions of LC. Of

430   the three remaining Fe(II)-bearing minerals, biotite was found to be the most important one for the generation of WIF in LC

431   (see also Buss et al., 2008; Bazilevskaya et al., 2013, 2015) due to its volumetric expansion during weathering (e.g.,

432   Goodfellow et al., 2016). Although WIF also occurs in NA (Fig. 4b) it does not seem to significantly increase the permeability

433   of the rock which can be related to the low Fe(II) content of the dominant bedrock (Fe_2O_3 (total Fe): <3 wt.%; Table S1; see

434   Kim et al., 2017).

435   Other than that, chlorite is suggested to be an important mineral in the development of the investigated weathering profile in

436   LC. The original chlorite content of the bedrock in LC has been completely transformed into interstratified chlorite-smectite

437   in the soil pit profile. We suggest that this transformation plays a significant role for the development of the LC profile since

438   expandable clay minerals are known to disaggregate rock by swelling (e.g., Dunn and Hudec, 1966; Jiménez-González et al.,

439   2008). The ensuing fracturing also forms new fluid pathways and new access to reactive surfaces of primary minerals which

440   in turn fosters weathering reactions (positive feedback mechanism; see e.g., Røyne et al., 2008). Even though expandable clay

441   minerals can also cause sealing of the subsurface (Kim et al., 2017) we do not regard this effect as significant for LC since

442   clay contents are very low. However, a minor retardation of the fluid flow from surface to depth due to the expansion of the

443   interstratified clay minerals in LC (Fig. 8a) cannot be excluded (see Kim et al., 2017). In conclusion, we propose that small

444   amounts of expandable clay minerals like in LC can generate porosity whereas high amounts of expandable clay minerals can

445   reduce porosity.

5.2.2 Increase of weathering intensity by biogenic activity

447   The formation of secondary minerals such as clay minerals and aluminium hydroxide is among other factors controlled by

448   biogenic activity since organic acids and an acidity-increase by elevated organic-derived CO_2 contents accelerate dissolution

449   rates of primary minerals (see e.g., Lucas, 2001; Lawrence et al., 2014). This effect needs to be considered for the organic-rich

450   and acidic subsurface of NA (see Bernhard et al., 2018). The acidity likely contributes to the high degree of mineral dissolution

451   in NA (see a_{H+} in Fig. 9), which consequently leads to an increased formation of secondary minerals.

452 The depth interval 120–140 cm in LC is characterized by lower amounts of biotite and a different clay mineral composition

453 compared to the surrounding depth intervals (Fig. 7b; Fig. 8a). This depth interval coincides with a discontinuity crossing the

454 entire profile width (Fig. 1d). We interpret this plant-root-containing discontinuity in the saprolite as a fracture remnant since

455 there are no indications of a lithological heterogeneity in this zone (e.g., a significant change in the magnetic susceptibility or

456 of the primary mineral content; Fig. 7b,c). To explain the lower biotite content and the different clay composition in this part

457 of the profile, we propose an intensification of weathering reactions in the vicinity of the fracture fostered by the observed

458 plant roots (e.g., Fimmen et al., 2008; Pawlik et al., 2016; Nascimento et al., 2021). This weathering-promoting mechanism

459 might account for the increase in interstratified chlorite-smectite and the appearance of interstratified mica-vermiculite (Fig.

460 8a), while the amount of biotite decreases due to its transformation to secondary minerals (Fig. 7b).

461 **5.3 Weathering-mitigating processes**

462 **5.3.1 O_2 consumption by Fe-bearing silicates and its impact on the weathering depth and intensity**

463 The granodiorite of LC hosts an abundance of Fe(II)-bearing minerals (Fig. 7b). The Fe_2O_3 content of the LC bedrock after

464 subtraction of the inert magnetite-bound Fe_2O_3 fraction (since 100 % pure magnetite contains 69 % Fe_2O_3, 0.94 % magnetite

465 as analysed in the LC bedrock equals to 0.65 % magnetite-bound Fe_2O_3 which needs to be subtracted) is 5.34 wt.% (for

466 comparison: 2.33 wt.% Fe_2O_3 in NA). Since O_2 is reduced by the oxidation of mineral-bound Fe(II) (e.g., White and Yee,

467 1985; Perez et al., 2005) and the consequent formation of secondary minerals, the O_2 content and hence oxidative weathering

468 reactions are expected to decrease from surface to depth. A rapid decrease of the O_2 concentration to depth is characteristic for

469 weathering systems in which O_2 transport is dominated by diffusion (Behrens et al., 2015). Given the observed deep fracturing

470 due to Fe(II) oxidation (i.e., WIF) in LC and the consequent deep connectivity between the surface and the subsurface (Kim

471 et al., 2017), the O_2 transport in LC is most likely dominated by advection. As a consequence, diffusive O_2 transport is

472 insignificant in the upper regolith of LC and the O_2 consumption by Fe(II) oxidation is not limiting the regolith depth in LC

473 (compare Bazilevskaya et al., 2013). The WIF-controlled connectivity between the surface and the subsurface results in an O_2

474 availability for oxidative weathering processes at great depth. On the other hand, the weak chemical weathering in LC is in

475 good agreement with the low precipitation rate (~350 mm yr^{-1}; Übernickel et al., 2020). The low precipitation rate entails a

476 small infiltration of water to depth and hence minor primary mineral dissolution and thus chemical weathering at depth.

477 The cracks around weathered biotite in the investigated samples of LC are (mainly) filled with Fe(III) oxyhydroxides as

478 revealed by the high Fe-enrichment detected in electron microprobe maps (Fig. 3d). Newly formed weathering-induced

479 fractures make the biotite more accessible to surface inputs like water and O_2 which promotes the dissolution of biotite. The

480 solutes formed as a result migrate along the weathering-induced cracks and precipitate in the vicinity of the biotite crystal as

481 secondary phases (Fig. 3c). Thus, we propose that the reactive surface of biotite is partly shielded from weathering reactants

482 (water, O_2) due to the precipitation of secondary minerals (see e.g., Navarre-Sitchler et al., 2015; Vázquez et al., 2016; Gerrits

483 et al., 2020; 2021). Combined with the low subsurface water availability in LC causing a low mineral dissolution degree, this

484 shielding might contribute to the relatively stable biotite content throughout the LC profile (Table S4).

485

5.3.2 Reduction of weathering intensity and -depth by damping of fluid flow

487 The formation of secondary minerals such as clay minerals (via amorphous and poorly crystalline precursors; see Fig. 6) can

488 decrease the porosity (e.g., Bazilevskaya et al., 2015; Navarre-Sitchler et al., 2015) formed by WIF and dissolution. Al-rich

489 phases were found as precipitates in partly dissolved plagioclase of NA (Fig. 4d–f) and within cracks which can often be

490 identified as weathering-induced. We suggest that the abundant presence of clay minerals and gibbsite in NA restricts the fluid

491 flow through such fractures and pores. The clay-rich zone in the uppermost metre of the NA soil pit profile (around 50 cm

492 depth; Fig. 7d) likely acts as a (partially) shielding horizon (impeding vertical flow of surface inputs to the deep subsurface;

493 see e.g., Lohse and Dietrich, 2005). Clay-rich horizons can therefore influence the dynamic of the subsurface fluid flow and

494 thus mitigate mineral transformations and chemical weathering at depth. However, the seasonal sealing of fractures and pore

495 spaces due to an increase of soil moisture and an ensuing clay expansion (Kim et al., 2017) is not assumed for NA as expandable

496 secondary minerals barely occur in the clay-size fraction of NA (Fig. 8b).

6 Conclusions

498 In two 6 m deep weathering profiles formed on granitic rock in two climatic zones (Mediterranean and humid climate), we

499 found different degrees of elemental loss by chemical weathering, and different secondary minerals. Under Mediterranean

500 climate conditions (La Campana), Fe(II)-oxidation, precipitation of Fe(III) oxyhydroxide and clay swelling lead to fracturing

501 and the formation of fluid pathways. This weathering-induced fracturing (WIF) is likely one of the dominant controls on the

502 development of the upper regolith as it leads to a deep infiltration of surface inputs (esp. water and O_2) which in turn causes

503 further WIF. While the intensity of chemical weathering at the Mediterranean site is low, it was detected throughout the entire

504 6 m deep profile. This suggests that the weathering front is located at much greater depth in La Campana. The overall low

505 abundance of secondary minerals can be explained by the low climate-related subsurface water availability in La Campana.

506 The lack of large quantities of secondary minerals ensures that fractures and porosity generated by WIF remain accessible to

507 water and gases. Thus, we conclude that the development of the deep but weak chemical weathering in the upper regolith of

508 La Campana is significantly controlled by two mechanisms: (1) A positive feedback loop between the formation of secondary

509 minerals and the infiltration of fluids to depth induced by (mainly) biotite weathering (WIF) which leads to a deep surface-

510 subsurface connectivity for weathering reactants (in particular O_2). (2) Low subsurface water availability resulting in a low

511 amount of secondary minerals which would otherwise seal this connectivity.

512 Under humid climate conditions (Nahuelbuta), clay minerals, gibbsite as well as amorphous and poorly crystalline secondary

513 minerals largely formed due to intense plagioclase dissolution. We link this intense dissolution to the high climate-related

514 subsurface water availability in Nahuelbuta. The secondary minerals thus formed are suggested to impede the flow of surface

515 inputs to depth. Moreover, the generally lower amount of Fe(II)-bearing silicates in Nahuelbuta compared to La Campana

516 results in less WIF and thus fewer fluid pathways. Therefore, we conclude that the development of the weathering profile in

517 Nahuelbuta is predominantly governed by two mechanisms: (1) Considerable climate-related subsurface water availability and

518 high biogenic activity which lead to intense weathering of primary minerals in the upper part of the regolith. (2) A negative

519 feedback loop between the formation of secondary minerals and the infiltration of fluids to depth induced by (mainly)

520 plagioclase weathering and the ensuing formation of secondary minerals which leads to a poor surface-subsurface connectivity

521 for weathering reactants.

522 This study illustrates how the formation of secondary minerals and the infiltration of surface-derived fluids to depth are

523 interlinked by positive and negative feedback loops. We demonstrated that these feedback loops and the climatic conditions

524 they occur in are important controls on the development of the upper regolith.

525

Data availability

527 Datasets related to this article can be found in the data publication Hampl et al. (2022b).

528 Review link:

529 https://dataservices.gfz-potsdam.de/panmetaworks/review/ef964dd7a2fee72ce4c235e97a324354c01091ad90e0f2837e0a937c96baa4f0/

530 The data publication is hosted at the GFZ Data Services and can be downloaded by clicking on "Download data and

531 description" in the field "Files".

532

Sample availability

534 The IGSN-registered samples used in this article are deposited at the Department of Applied Geochemistry (Technische

535 Universität Berlin) and are listed in the data publication of this paper (Hampl et al., 2022b).

536

Author contribution

538 Ferdinand J. Hampl: conceptualization, methodology, investigation, writing – original draft preparation

539 Ferry Schiperski: methodology, supervision, writing – review & editing

540 Christopher Schwerdhelm: investigation, writing – review & editing

541 Nicole Stroncik: investigation, writing – review & editing

542 Casey Bryce: funding acquisition, writing – review & editing

Earth **Surface**
Dynamics
Discussions
Open Access

EGU

543 Friedhelm von Blanckenburg: supervision, writing – review & editing

544 Thomas Neumann: funding acquisition, supervision, writing – review & editing

545

546 **Competing interests**

547 The authors declare that they have no conflict of interest.

548

556 **References**

557 Anderson, S., Dietrich, W., and Brimhall, G.: Weathering profiles, mass-balance analysis, and rates of solute loss: Linkages

558 between weathering and erosion in a small, steep catchment, Geol. Soc. Am. Bull., 114 (9), 1143–1158,

559 https://doi.org/10.1130/0016-7606(2002)114<1143:WPMBAA>2.0.CO;2, 2002.

560 Anovitz, L.M., Cheshire, M.C., Hermann, R.P., Gu, X., Sheets, J.M., Brantley, S.L., Cole, D.R., Ilton, E.S., Mildner, D.F.R.,

561 Gagnon, C., Allard, L.F., and Littrell, K.C.: Oxidation and associated pore structure modification during experimental

562 alteration of granite, Geochim. Cosmochim. Ac., 292, 532–556, https://doi.org/10.1016/j.gca.2020.08.016, 2021.

563 Bandstra, J. Z., Buss, H. L., Campen, R. K., Liermann, L. J., Moore, J., Hausrath, E. M., Navarre-Sitchler, A. K., Jang, J.-H.,

564 and Brantley, S. L.: Compilation of mineral dissolution rates, in: Kinetics of Water-Rock Interaction, edited by: Brantley, S.

565 L., Kubicki, J. D., and White, A. F., Springer New York, 737–823, https://doi.org/10.1007/978-0-387-73563-4, 2008.

566 Bazilevskaya, E., Lebedeva, M., Pavich, M., Rother, G., Parkinson, D. Y., Cole, D., and Brantley, S. L.: Where fast weathering

567 creates thin regolith and slow weathering creates thick regolith, Earth Surf. Proc. Land., 38, 847–858,

568 https://doi.org/10.1002/esp.3369, 2013.

569 Bazilevskaya, E., Rother, G., Mildner, D. F., Pavich, M., Cole, D., Bhatt, M. P., Jin, L., Steefel, C. I., and Brantley, S. L.: How
570 Oxidation and Dissolution in Diabase and Granite Control Porosity during Weathering, Soil Sci. Soc. Am. J., 79, 55–73,
571 https://doi.org/10.2136/sssaj2014.04.0135, 2015.

572 Behrens, R., Bouchez, J., Schuessler, J. A., Dultz, S., Hewawasam, T., and von Blanckenburg, F.: Mineralogical
573 transformations set slow weathering rates in low-porosity metamorphic bedrock on mountain slopes in a tropical climate,
574 Chem. Geol., 411, 283–298, https://doi.org/10.1016/j.chemgeo.2015.07.008, 2015.

575 Behrens, R., Wirth, R., and von Blanckenburg, F.: Rate limitations of nano-scale weathering front advance in the slow-eroding
576 Sri Lankan Highlands, Geochim. Cosmochim. Ac., 311, 174–197, https://doi.org/10.1016/j.gca.2021.06.003, 2021.

577 Bernhard, N., Moskwa, L.-M., Schmidt, K., Oeser, R. A., Aburto, F., Bader, M. Y., Baumann, K., von Blanckenburg, F., Boy,
578 J., van den Brink, L., Brucker, E., Büdel, B., Canessa, R., Dippold, M. A., Ehlers, T. A., Fuentes, J. P., Godoy, R., Jung, P.,
579 Karsten, U., Köster, M., Kuzyakov, Y., Leinweber, P., Neidhardt, H., Matus, F., Mueller, C. W., Oelmann, Y., Oses, R., Osses,
580 P., Paulino, L., Samolov, E., Schaller, M., Schmid, M., Spielvogel, S., Spohn, M., Stock, S., Stroncik, N., Tielbörger, K.,
581 Übernickel, K., Scholten, T., Seguel, O., Wagner, D., and Kühn, P.: Pedogenic and microbial interrelations to regional climate
582 and local topography: New insights from a climate gradient (arid to humid) along the Coastal Cordillera of Chile, CATENA,
583 170, 335–355, https://doi.org/10.1016/j.catena.2018.06.018, 2018.

584 Buss, H. L., Sak, P. B., Webb, S. M., and Brantley, S. L.: Weathering of the Rio Blanco quartz diorite, Luquillo mountains,
585 Puerto Rico: coupling oxidation, dissolution, and fracturing, Geochim. Cosmochim. Ac., 72, 4488–4507,
586 https://doi.org/10.1016/j.gca.2008.06.020, 2008.

587 Chesworth W. et al.: Clay Mineral Formation, in: Encyclopedia of Soil Science, Encyclopedia of Earth Sciences Series, edited
588 by: Chesworth, W., Springer, Dordrecht, Figure C51, https://doi.org/10.1007/978-1-4020-3995-9_108, 2008.

589 Dawson, T. E., Hahm, W. J., and Crutchfield-Peters, K.: Digging deeper: what the critical zone perspective adds to the study
590 of plant ecophysiology, New Phytol., 226, 666–671, https://doi.org/10.1111/nph.16410, 2020.

591 Deckart, K., Hervé, F., Fanning, C., Ramírez, V., Calderón, M., and Godoy, E.: U-Pb Geochronology and Hf-O Isotopes of
592 zircons from the Pennsylvanian Coastal Batholith, South-Central Chile, Andean Geol., 41 (1), 49–82,
593 https://doi.org/10.5027/andgeoV41n1-a03, 2013.

594 Drever, J. I.: The effect of land plants on weathering rates of silicate minerals, Geochim. Cosmochim. Ac., 58, 2325–2332,
595 https://doi.org/10.1016/0016-7037(94)90013-2, 1994.

596   Dunn, J. R., and Hudec, P. P.: Water, Clay and Rock Soundness, Ohio J. Sci., 66 (2), 153–168, 1966.

597   Ferraris, F.: Hoja Los Angeles – Angol, Escala: 1:250.000, Carta Geológica de Chile N°5 (Preliminar), Instituto de
598   Investigaciones Geológicas, OCLC number: 1024799672, 1979.

599   Ferré, E., Michelsen, K., Ernst, W., Boyd, J., and Cañón-Tapia, E.: Vertical zonation of the Barcroft granodiorite, White
600   Mountains, California: Implications for magmatic processes, Am. Mineral., 97, 1049–1059, https://doi.org/1049-1059.
601   10.2138/am.2012.4013, 2012.

602   Fimmen, R., Richter, D., Vasudevan, D., Williams, M., and West, L.: Rhizogenic Fe-C redox cycling: A hypothetical
603   biogeochemical mechanism that drives crustal weathering in upland soils, Biogeochemistry, 87, 127–141,
604   https://doi.org/10.1007/s10533-007-9172-5, 2008.

605   Fletcher, R. C., Buss, H. L., and Brantley, S. L.: A spheroidal weathering model coupling porewater chemistry to soil
606   thicknesses during steady-state denudation, Earth Planet. Sc. Lett., 244, 444–457, https://doi.org/10.1016/j.epsl.2006.01.055,
607   2006.

608   Gana, P., Wall, R., and Gutiérrez, A.: Mapa geológico del área de Valparaiso-Curacavi, Región de Valparaiso y Región
609   Metropolitana, Mapas Geológicos, N° 1, Escala 1:100 000, Servicio Nacional de Geologia y Mineria (Chile), OCLC number:
610   43901854, 1996.

611   Gerrits, R., Pokharel, R., Breitenbach, R., Radnik, J., Feldmann, I., Schuessler, J. A., von Blanckenburg, F., Gorbushina, A.
612   A., and Schott, J.: How the rock-inhabiting fungus K. petricola A95 enhances olivine dissolution through attachment, Geochim.
613   Cosmochim. Ac., 282, 76–97, https://doi.org/10.1016/j.gca.2020.05.010, 2020.

614   Gerrits, R., Wirth, R., Schreiber, A., Feldmann, I., Knabe, N., Schott, J., Benning, L. G., and Gorbushina, A. A.: High-
615   resolution   imaging   of   fungal   biofilm-induced   olivine   weathering,   Chem.   Geol.,   559,   119902,
616   https://doi.org/10.1016/j.chemgeo.2020.119902, 2021.

617   Glodny, J., Echtler, H., Collao, S., Ardiles, M., Buron, P., and Figueroa, O.: Differential Late Paleozoic active margin evolution
618   in   South-Central   Chile   (37°   S–40°   S)   –   the   Lanalhue   Fault   Zone.   J.   S.   Am.   Earth   Sci.,   26,   397–411,
619   https://doi.org/10.1016/j.jsames.2008.06.001, 2008a.

620   Glodny, J., Gräfe, K., Echtler, H., and Rosenau, M.: Mesozoic to Quaternary continental margin dynamics in south-central
621   Chile   (36–42°S):   The   apatite   and   zircon   fission   track   perspective,   Int.   J.   Earth   Sci.,   97,   1271–1291,
622   https://doi.org/10.1007/s00531-007-0203-1, 2008b.

623 Goodfellow, B. W., Hilley, G. E., Webb, S. M., Sklar, L. S., Moon, S., and Olson, C. A.: The chemical, mechanical, and
624 hydrological evolution of weathering granitoid, J. Geophys. Res.-Earth, 121, 1410–1435,
625 https://doi.org/10.1002/2016JF003822, 2016.

626 Hampl, F. J., Schiperski, F., Byrne, J. M., Schwerdhelm, C., Kappler, A., Bryce, C., von Blanckenburg, F., and Neumann, T.:
627 The role of iron-bearing minerals for the deep weathering of a hydrothermally altered plutonic rock in semi-arid climate
628 (Chilean Coastal Cordillera), Chem. Geol., 604, 120922, https://doi.org/10.1016/j.chemgeo.2022.120922, 2022a.

629 Hampl, F. J., Schiperski, F., Schwerdhelm, C., Stroncik, N., Bryce, C., von Blanckenburg, F., and Neumann, T.: Mineralogical
630 and geochemical data of two weathering profiles in a Mediterranean and a humid climate region of the Chilean Coastal
631 Cordillera, GFZ Data Services [data set], https://doi.org/10.5880/fidgeo.2022.035, 2022b.

632 Hayes, N. R., Buss, H. L., Moore, O. W., Krám, P., and Pancost, R. D.: Controls on granitic weathering fronts in contrasting
633 climates, Chem. Geol., 535, 119450, https://doi.org/10.1016/j.chemgeo.2019.119450, 2020.

634 Hellmann, R., Wirth, R., Daval, D., Barnes, J.-P., Penisson, J.-M., Tisserand, D., Epicier, T., Florin, B., and Hervig, R. L.:
635 Unifying natural and laboratory chemical weathering with interfacial dissolution–reprecipitation: A study based on the
636 nanometer-scale chemistry of fluid–silicate interfaces, Chem. Geol., 294–295, 203–216,
637 https://doi.org/10.1016/j.chemgeo.2011.12.002, 2012.

638 Hervé, F.: Petrology of the crystalline basement of the Nahuelbuta Mountains, southcentral Chile, in: Comparative Studies on
639 the Geology of the Circum-Pacific Orogenic Belt in Japan and Chile, edited by: Ishikawa, T., and Aguirre, I., Japan Society
640 for the Promotion of Science, Tokyo, 1-51, 1977.

641 Holbrook, S., Marcon, V., Bacon, A., Brantley, S., Carr, B., Flinchum, B., Richter, D., and Riebe, C.: Links between physical
642 and chemical weathering inferred from a 65-m-deep borehole through Earth's critical zone, Sci. Rep.-UK, 9, 4495,
643 https://doi.org/10.1038/s41598-019-40819-9, 2019.

644 Holmgren, G. G. S.: A Rapid Citrate-Dithionite Extractable Iron Procedure, Soil Sci. Soc. Am. J., 31, 210–211,
645 https://doi.org/10.2136/sssaj1967.03615995003100020020x, 1967.

646 Hynek, S., Comas, X., and Brantley, S. L.: The effect of fractures on weathering of igneous and volcaniclastic sedimentary
647 rocks in the Puerto Rican tropical rain forest, Proced. Earth Plan. Sc., 17, 972–975,
648 https://doi.org/10.1016/j.proeps.2017.01.001, 2017.

649 Israeli, Y., Salhov, E., and Emmanuel, S.: Impact of textural patterns on modeled rock weathering rates and size distribution
650 of weathered grains, Earth Surf. Proc. Land., 46, 1177–1187, https://doi.org/10.1002/esp.5093, 2021.

651 Jiménez-González, I., Rodríguez-Navarro, C., and Scherer, G. W.: Role of clay minerals in the physicomechanical
652 deterioration of sandstone, J. Geophys. Res., 113, F02021, https://doi.org/10.1029/2007JF000845, 2008.

653 Jobbágy, E. G., and Jackson, R. B.: The uplift of soil nutrients by plants: biogeochemical consequences across scales, Ecology,
654 85, 2380–2389, https://doi.org/10.1890/03-0245, 2004.

655 Kim, H., Stinchcomb, G., and Brantley, S.: Feedbacks among O_2 and CO_2 in deep soil gas, oxidation of ferrous minerals, and
656 fractures: A hypothesis for steady-state regolith thickness, Earth Planet. Sc. Lett., 460, 29–40,
657 https://doi.org/10.1016/j.epsl.2016.12.003, 2017.

658 Kogure, T., and Banfield, J. F.: New insights into the mechanism for chloritization of biotite using polytype analysis, Am.
659 Mineral., 85 (8–9), 1202–1208, https://doi.org/10.1515/am-2000-8-913, 2000.

660 Krone, L. V., Hampl, F. J., Schwerdhelm, C., Bryce, C., Ganzert, L., Kitte, A., Übernickel, K., Dielforder, A., Aldaz, S., Oses-
661 Pedraza, R., Perez, J. P. H., Sanchez-Alfaro, P., Wagner, D., Weckmann, U., and von Blanckenburg, F.: Deep weathering in
662 the semi-arid Coastal Cordillera, Chile, Sci. Rep.-UK, 11, 13057, https://doi.org/10.1038/s41598-021-90267-7, 2021.

663 Lawrence, C., Harden, J., and Maher, K.: Modeling the influence of organic acids on soil weathering, Geochim. Cosmochim.
664 Ac., 139, 487–507, https://doi.org/10.1016/j.gca.2014.05.003, 2014.

665 Lebedeva, M. I., Fletcher, R. C., Balashov, V. N., and Brantley, S. L.: A reactive diffusion model describing transformation
666 of bedrock to saprolite, Chem. Geol., 244, 624–645, https://doi.org/10.1016/j.chemgeo.2007.07.008, 2007.

667 Lohse, K. A., and Dietrich, W. E.: Contrasting effects of soil development on hydrological properties and flow paths, Water
668 Resour. Res., 41, W12419, https://doi.org/10.1029/2004WR003403, 2005.

669 Lucas, Y.: The Role of Plants in Controlling Rates and Products of Weathering: Importance of Biological Pumping, Annu.
670 Rev. Earth Pl. Sc., 29, 135–163, https://doi.org/10.1146/annurev.earth.29.1.135, 2001.

671 Luebert, F., and Pliscoff, P.: Sinópsis bioclimática y vegetacional de Chile, Editorial Universitaria, Santiago de Chile, ISBN
672 956-11-1832-7, 2006.

673 McKeague, J. A., and Day, J. H.: Dithionite- and oxalate-extractable Fe and Al as aids in differentiating various classes of
674 soils, Can. J. Soil Sci., 46 (1), 13–22, https://doi.org/10.4141/cjss66-003, 1966.

675 Melnick, D.: Rise of the central Andean coast by earthquakes straddling the Moho, Nat. Geosci., 9, 401–407,
676 https://doi.org/10.1038/ngeo2683, 2016.

677 Molnar, P., Anderson, R. S., and Anderson, S. P.: Tectonics, fracturing of rock, and erosion, J. Geophys. Res., 112, F03014,
678 https://doi.org/10.1029/2005JF000433, 2007.

679 Nadan, B. J., and Engelder, T.: Microcracks in New England granitoids: A record of thermoelastic relaxation during
680 exhumation of intracontinental crust, Geol. Soc. Am. Bull., 121, 80–99, https://doi.org/10.1130/b26202.1, 2009.

681 Napieralski, S. A., Buss, H. L., Brantley, S. L., Lee, S., Xu, H., and Roden, E. E.: Microbial chemolithotrophy mediates
682 oxidative weathering of granitic bedrock, P. Natl. Acad. Sci. USA, 116, 26394–26401,
683 https://doi.org/10.1073/pnas.1909970117, 2019.

684 Nascimento, D. L., Abrahão, A., Lambers, H., Teodoro, G. S., Ladeira, F. S. B., de Britto Costa, P., Oliveira, R. S., and de
685 Farias, C. H. B.: Biogeomorphological evolution of rocky hillslopes driven by roots in campos rupestres, Brazil,
686 Geomorphology, 395, 107985, https://doi.org/10.1016/j.geomorph.2021.107985, 2021.

687 Navarre-Sitchler, A., Brantley, S. L., and Rother, G.: How Porosity Increases During Incipient Weathering of Crystalline
688 Silicate Rocks, Rev. Mineral. Geochem., 80 (1), 331–354, https://doi.org/10.2138/rmg.2015.80.10, 2015.

689 Nesbitt, H., and Young, G.: Early Proterozoic climates and plate motions inferred from major element chemistry of lutites,
690 Nature, 299, 715–717, https://doi.org/10.1038/299715a0, 1982.

691 Oeser, R. A., Stroncik, N, Moskwa, L.-M., Bernhard, N., Schaller, M., Canessa, R., van den Brink, L., Köster, M., Brucker,
692 E., Stock, S., Fuentes, J. P., Godoy, R., Matus, F. J., Oses Pedraza, R., Osses McIntyre, P., Paulino, L., Seguel, O., Bader, M.
693 Y., Boy, J., Dippold, M. A., Ehlers, T. A., Kühn, P., Kuzyakov, Y., Leinweber, P., Scholten, T., Spielvogel, S., Spohn, M.,
694 Übernickel, K., Tielbörger, K., Wagner, D., and von Blanckenburg, F.: Chemistry and microbiology of the Critical Zone along
695 a steep climate and vegetation gradient in the Chilean Coastal Cordillera, CATENA, 170, 183–203,
696 https://doi.org/10.1016/j.catena.2018.06.002, 2018.

697 Oeser, R. A., and von Blanckenburg, F.: Do degree and rate of silicate weathering depend on plant productivity?
698 Biogeosciences, 17, 4883–4917, https://doi.org/10.5194/bg-17-4883-2020, 2020.

699 Pawlik, Ł., Phillips, J. D., and Šamonil, P.: Roots, rock, and regolith: Biomechanical and biochemical weathering by trees and
700 its impact on hillslopes – A critical literature review, Earth-Sci. Rev., 159, 142–159,
701 https://doi.org/10.1016/j.earscirev.2016.06.002, 2016.

702 Perez, J. R., Banwart, St. A., and Puigdomenech, I.: The kinetics of $O_{2(aq)}$ reduction by structural ferrous iron in naturally
703 occurring ferrous silicate minerals, Appl. Geochem., 20, 2003–2016, https://doi.org/10.1016/j.apgeochem.2005.07.001, 2005.

704 Rempe, D. M., and Dietrich, W. E.: A bottom-up control on fresh-bedrock topography under landscapes, P. Natl. Acad. Sci.
705 USA, 111 (18), 6576–6581, https://doi.org/10.1073/pnas.1404763111, 2014.

706 Rennert, T.: Wet-chemical extractions to characterise pedogenic Al and Fe species – a critical review, Soil Res., 57, 1–16,
707 https://doi.org/10.1071/SR18299, 2019.

708 Riebe, C. S., Kirchner, J. W., and Finkel, R. C.: Long-term rates of chemical weathering and physical erosion from cosmogenic
709 nuclides and geochemical mass balance, Geochim. Cosmochim. Ac., 67, 4411–4427, https://doi.org/10.1016/S0016-
710 7037(03)00382-X, 2003.

711 Røyne, A., Jamtveit, B., Mathiesen, J., and Malthe-Sørenssen, A.: Controls on rock weathering rates by reaction-induced
712 hierarchical fracturing, Earth Planet. Sc. Lett., 275, 364–369, https://doi.org/10.1016/j.epsl.2008.08.035, 2008.

713 Schneider, C. A., Rasband, W. S., and Eliceiri, K. W.: NIH Image to ImageJ: 25 years of image analysis, Nat. Methods, 9 (7),
714 671–675, https://doi.org/10.1038/nmeth.2089, 2012.

715 Schwertmann, U.: Differenzierung der Eisenoxide des Bodens durch Extraktion mit Ammoniumoxalat-Lösung, Zeitschrift für
716 Pflanzenernährung, Düngung, Bodenkunde, 105, 194–202, https://doi.org/10.1002/jpln.3591050303, 1964.

717 Starkey, H. C., Blackmon P. D., and Hauff P. L. The routine mineralogical analysis of clay-bearing samples, U.S. Geological
718 Survey Bulletin, 1563, https://doi.org/10.3133/b1563, 1984.

719 St. Clair, J., Moon, S., Holbrook, W. S., Perron, J. T., Riebe, C. S., Martel, S. J., Carr, B., Harman, C., Singha, K., and Richter,
720 D.: Geophysical imaging reveals topographic stress control of bedrock weathering, Science, 350 (6260), 534–538,
721 https://doi.org/10.1126/science.aab2210, 2015.

722 Steefel, C. I., and van Cappellen, P.: A new kinetic approach to modeling water-rock interaction: The role of nucleation,
723 precursors, and Ostwald ripening, Geochim. Cosmochim. Ac., 54 (10), 2657–2677, https://doi.org/10.1016/0016-
724 7037(90)90003-4, 1990.

725 Steenken, A., Rabbia, O., and Hernández, L.: The Emplacement of the Nahuelbuta Batholith in an Active Continental Margin
726 (Central Chile), XVIII Congreso Peruano de Geología, Lima, Peru, 2016.

727 Übernickel, K., Ehlers, T. A., Ershadi, M. R., Paulino, L., Fuentes Espoz, J.-P., Maldonado, A., Oses-Pedraza, R., and von
728 Blanckenburg, F.: Time series of meteorological station data in the EarthShape study areas in the Coastal Cordillera, Chile,
729 GFZ Data Services [data set], https://doi.org/10.5880/fidgeo.2020.043, 2020.

730 van Dongen, R., Scherler, D., Wittmann, H., and von Blanckenburg, F.: Cosmogenic 10Be in river sediment: where grain size
731 matters and why, Earth Surf. Dynam., 7, 393–410, https://doi.org/10.5194/esurf-7-393-2019, 2019.

732 Vázquez, M., Ramírez, S., Morata, D., Reich, M., Braun, J.-J., and Carretier, S.: Regolith production and chemical weathering
733 of granitic rocks in central Chile, Chem. Geol., 446, 87–98, https://doi.org/10.1016/j.chemgeo.2016.09.023, 2016.

734 Werner, C., Schmid, M., Ehlers, T. A., Fuentes-Espoz, J. P., Steinkamp, J., Forrest, M., Liakka, J., Maldonado, A., and Hickler,
735 T.: Effect of changing vegetation and precipitation on denudation – Part 1: Predicted vegetation composition and cover over
736 the last 21 thousand years along the Coastal Cordillera of Chile, Earth Surf. Dynam., 6, 829–858, https://doi.org/10.5194/esurf-
737 6-829-2018, 2018.

738 White, A. F., and Yee, A.: Aqueous oxidation-reduction kinetics associated with coupled electron transfer from iron-containing
739 silicates at 25°C, Geochim. Cosmochim. Ac., 49, 1263–1275, https://doi.org/10.1016/0016-7037(85)90015-8, 1985.

740 Wilson, M. J.: Weathering of the primary rock-forming minerals: processes, products and rates, Clay Miner., 39, 233–266,
741 https://doi.org/10.1180/0009855043930133, 2004.